University of Twente
Faculty of Science & Technology

Master Thesis

MR-imaging of the prostate: diagnosis and treatment improvement

Author:
J. Heidkamp BSc

Supervisors:
prof. dr. I.A.M.J. Broeders
dr. J.J. Fütterer
dr. ir. F. van der Heijden
prof. dr. ir. C.H. Slump
drs. P.A. van Katwijk

A thesis submitted in fulfilment of the requirements for the degree of Master of Science

in

Technical Medicine

October 6, 2015

UNIVERSITY OF TWENTE.

Radboudumc
university medical center

Preface

Before you lies my thesis which was written in order to obtain the Master of Science degree in Technical Medicine, with a specialisation in Medical Imaging and Interventions, from the faculty of Science & Technology at the University of Twente in Enschede. It presents the research conducted at the department of Radiology and Nuclear Medicine of the Radboudumc in Nijmegen during the clinical specialization internship in the final year of education.

Several persons have contributed to the realization of this thesis whom therefore deserve acknowledgement. First of all, I would like to express my gratitude to Jurgen, Ferdi, and Paul for their medical, technical, and process supervision. I would like to thank my direct colleague's Joyce, Kristian, Martijn, Martin, Tim, and Wulphert for either scientific support or their support at gaining clinical experience. Furthermore, I thank my fellow clinical technologists, Charlotte, Stefan, Suzan and Willem for supporting me with their experience of the graduation process.

Finally, I would like to thank my family, friends, and Myrte for always showing genuine interest.

Jan Heidkamp
Nijmegen, September 16, 2015

Contents

List of Figures

List of Tables

Part I

General introduction

Chapter 1

Purpose and structure of this thesis

The purpose of this thesis was to investigate prostate MR-imaging solutions that intend to improve the diagnosis and treatment of prostate cancer. In total, a number of two techniques/methods were studied. At first the application of an in-room mobile touching device (MTD) to monitor and target MR-guided prostate biopsies (MRGB) were examined. The goal of applying an in-room MTD is to increase the efficiency of the time-consuming MR biopsy procedure. First, the MR-safety and compatibility of the MTD were investigated, the next steps were to validate the method a) in a phantom and b) on the patient. The major endpoints of this study were improved efficiency, i.e. time reduction of the procedure and equal or possibly better accuracy of the biopsies.

The second project in thesis focused on the treatment improvement of prostate cancer. The goal of the project was to examine whether ex vivo prostate MR is a feasible means to identify positive surgical margins (PSM) in a radical prostatectomy specimen. If feasible, ex vivo MRI might be a faster solution for determining potential positive resection margins compared to a pathologist's determination. Moreover, this technique could be employed to direct extended resection or radiation therapy while the patient is still on the operation table.

Initially, the execution of third project was intended in which a MR compatible biospy robot* was going to be evaluated. However, due to a delay in the development of the robot itself the project did not fit into the time scope of the internship any more. Therefore, inclusion of the project into this thesis was renounced.

The resulting thesis consists of three main parts. Part I introduces the subject of prostate cancer and MR imaging of the prostate as well as the treatment of prostate cancer in chapter 2. Part II contains the research that was performed within the scope of the application of an in-room MTD to monitor and target MRGB. It consists of four chapters (chapter 3-6) that together intend to form part of a scientific paper. Chapter 3 and 6 respectively present a scientific introduction and method that are going to be implemented into a publication. However, the work presented in chapter 4

*The MIRIAM project: `http://cmi-nen.nl/business/projects/miriam/`

and 5 is written in a report-ish form which is suitable for including it into this thesis but not for scientific paper. The experiments described in these chapters will appear as paragraphs in the method section of the future publication and are already included as such in chapter 6. Part II does not contain the results of the aforementioned patient study that we intended to conduct as a result of the Institutional Review Board application that had to be done first. At the moment of writing, the patient study is postponed awaiting the Board's verdict so the actual conduction is future work. Part III contains only one chapter, chapter 7, that presents the high field MRI ex vivo prostate study. This work is presented as a scientific paper that is going to be published. Chapter 8 summarizes the conclusions from this thesis as a separate chapter. Finally, three appendices are presented containing specific descriptions of methods that were used during the experiments of chapter 4 and 5.

Chapter 2

Background

2.1 Prostate cancer

The prostate is an exocrine gland which is part of the male reproductive system. It situated just below the urinary bladder in which it surrounds the urethra and its main function is to secrete a slightly alkaline fluid that is part of the semen. Four different zones of the prostate gland can be distinguished. The peripheral zone is located in the posterior part of the gland closest to the rectum. This is the zone where most prostate cancers (PCa) (74%) originate from [1] . The transition zone is the innermost part of the prostate surrounding the proximal urethra, 23% of PCa originate here [1]. It begins to enlarge as men pass age 40, a disease referred to as benign prostatic hyperplasia (BPH). Lastly the prostate consists of the central zone surrounding the ejaculatory ducts and the anterior fibromuscular zone.

In the Netherlands 10,897 men were diagnosed with prostate cancer in 2013 of the total of 53,095 men diagnosed with cancer of all sites but non-melanoma skin [2]. Almost half (47%) of the men diagnosed with PCa is 70 years or older [2]. In that same year 2,535 men died of prostate cancer among the total of 23,054 cancer related deaths, with that it is the second most common cancer related death cause in the Netherlands after trachea- and lung cancer [2, 3]. It is estimated that absolute incidence of prostate cancer will increase to 17,000 new patients a year in 2020 which is mainly attributable to the ageing population [4].

The clinical behaviour of prostate cancer ranges from a microscopic, well differentiated tumour that may never clinically significant to an aggressive, high grade cancer that ultimately causes metastases, morbidity and death [5]. Symptoms attributable to cancer are absent in most men with early state prostate cancer. Some symptoms that could be associated with prostate cancer and are seen commonly are urinary frequency, urgency, nocturia, and hesitancy, but could be related to BPH as well. Less common are hematuria and hematospermia, both symptoms that are more likely to be caused by BPH than cancer.

Several screening tests are available that lead to the suspicion on prostate cancer, however only a biopsy of a suspected lesion can fully diagnose and stage prostate cancer. On digital rectal examination (DRE) a physician palpates the prostate to search for irregularities. However, this technique is not an accurate staging method, because benign and malignant nodules are hard to be distinguished from each other [6]. Furthermore, the test is liable to inter observer variability [7]. Another available test is the examination of the serum prostate specific antigen (PSA). The PSA protein is highly specific for the prostate as it is excreted solely by prostate cells. Yet, it is not prostate cancer specific, because other conditions such as BPH or prostatitis can also cause an elevated PSA level. Despite the fact that this test lacks prostate cancer specificity, more prostate cancers are detected as a result of the widespread PSA screening, because men with a suspicious serum PSA undergo a biopsy [5].

In case of a suspicious DRE and/or PSA level a biopsy of the prostate should be performed in order to further evaluate the diagnosis. The most commonly used technique for that is a transrectal ultrasound guided biopsy [8]. However, the major drawback of this is method is its low prostate cancer detection rate of 22% [9], because of the fact that more than 40% of prostate tumours are isoechoic and only the peripheral zone can be accurately detected [10]. Furthermore, the technique is associated with a significant false negative rate ranging between 20% and 33% [11]. As a result of these limitations, many patients with a persistently elevated or rising PSA and negative TRUS biopsies are subject to diagnostic uncertainty.

2.2 MR prostate imaging

An answer to these limitations is the increasing role of MR imaging in the detection of prostate cancer. Unlike ultrasound, MRI has a high sensitivity for detecting prostate tumours and provides excellent soft tissue contrast and multiplanar volumetric imaging capabilities [12]. A study showed overall accuracies of 67%-69% of T2 weighted imaging in localizing prostate cancer with a 1.5 T MR scanner [13]. The same study also showed that the use of functional MR further increased the detecting accuracy. The application of dynamic contrast enhanced (DCE) and MR spectroscopic images in conjunction with the T2 weighted images resulted in accuracies of 91% and 81% respectively [13]. Another functional MR technique is diffusion weighted imaging (DWI) and a combination of diffusion weighted and T2 weighted images showed areas under the receiver operating curve of 0.92 and 0.88 for the peripheral and transition zone respectively [14].

Instead of using TRUS to guide the biopsies, the created by means of MR can be used to guide them. Currently available data, shows that in patients with prior negative TRUS guided biopsy results, 3 T MR guided prostate biopsy is feasible and has a higher detection rate than does repeat TRUS guided biopsy [10, 15]. In our institution, a transrectal biopsy of the prostate is taken under MR guidance with the assistance of previously acquired diagnostic MR images (T2 weighted, DWI and DCE). The transrectal approach provides a short pathway in which no anaesthetics are required.

The biopsy session starts with acquiring T2 and diffusion weighted images of the prostate once more to verify the position of the lesions. Subsequently, a needle guided which is visible on T2 weighted images is inserted rectally. The guide is connected to an MR compatible biopsy device (Invivo, Schwerin, Germany) that enables rotation, angulation and translation of the MR compatible biopsy needle. A localizer image is used to detect and reposition the needle whereupon MR images in two perpendicular planes must be obtained to direct the needle guide to the target. Once the needle guide and the suspected lesion are aligned the needle can be slid through and a biopsy can be obtained for pathological analysis.

2.3 Treatment of prostate cancer

Several treatment options exist for men with localized prostate cancer (clinically confined to the prostate) including radical prostatectomy (RP), external beam radiotherapy (EBRT), interstitial prostate brachytherapy, hormonal therapy, combinations of these, and active surveillance (AS). The most important factors in selecting the initial treatment are, the histological grade (Gleason score), clinical TNM stage, serum PSA level, life expectancy, comorbidities, and patient preference. For patients with low- and intermediate risk localized PCa (cT1a-T2 and Gleason score 6-7 and PSA $\leq$20) and a life expectancy of more than 10 years the recommended treatment is RP [16]. A prospective randomized control study, with a maximum follow-up of 23 years (median 13 years), demonstrated that in this category of patients, RP significantly lowered the incidence of death from all causes (56 versus 69%), death from PCa (18 versus 29%), distant metastases (26 versus 38%), and use of hormonal therapy (43 versus 67%) compared with AS [17]. Radical prostatectomy involves the removal of the entire prostate gland including seminal vesicles and the ampulla of the vas deferens. Depending on the characteristics of the tumour and the man's sexual function, this may invovle sparing of the neurovascular bundle increasing the chance on preservation of potency.

Part II

In-room monitoring and targeting of MR guided prostate biopsies

Chapter 3

Real-time MR guided prostate biopsies using a mobile touching device: introduction to a patient study

A persistently elevated or rising serum prostate specific antigen (PSA) level or an abnormal digital rectal examination (DRE) could indicate the presence of prostate cancer (PCa). However, the definite diagnosis of PCa depends on prostatic needle biopsies as they allow histopathologic confirmation [18]. The standard method to obtain material for histopathologic evaluation is the transrectal of transperineal ultrasound-guided systematic 12-core prostate biopsy [19,20]. Although the latter methods show a similar efficacy, the transrectal approach is the preferable route because it does not require spinal anaesthesia or catheterization [19]. Nevertheless, the transrectal ultrasound guided biopsy (TRUSGB) procedure is characterised by a low sensitivity (39-52%) and a relatively high specificity (81-82%) [21]. Moreover, detection rates diminish when patients are subjected to consecutive biopsies (10%, 5% and 4% for the second, third and fourth biopsies respectively) [9]. Furthermore, this method shows a significant discordance between the biopsy Gleason score and the underlying pathologic Gleason score: approximately one in three biopsy diagnoses of low grade cancers (Gleason 6) are upgraded at pathology [22]. Ultrasound is merely able to guide the physician to the gland itself while only the outlines of the organ are visible and local tissue characteristics are not. The physician has to determine the systematic biopsy sites by cognitively sub-dividing the gland into 12 symmetric locations. Consequently, the prostate is biopsied virtual blindly in contrast to all other image-based cancer diagnoses that are targeted by either direct (e.g. bronchoscopy) or radiologic imaging.

Compared to other imaging methods, magnetic resonance imaging (MRI) provides the best visuali-

sation of the prostate due to its inherent high soft-tissue contrast, high resolution, multi-planar volumetric capabilities, and the ability to simultaneously image functional parameters. Multi-parametric MRI (mpMRI) with T2-weighted (T2W), functional diffusion weighted imaging (DWI) and dynamic contrast enhanced (DCE) sequences is now the established approach to prostate MRI [23]. A recent meta-analysis reported pooled sensitivity and specificity of 0.74 and 0.88 respectively for mpMRI to detect clinically significant PCA [24]. Besides accurate detection of disease, mpMRI is able to perform accurate localisation of lesions. In a study conducted by Turkbey et al. [25], histopathological specimens were sliced exactly according to the mpMRI images by using a customised three-dimensional mould enabling standardised slicing. A positive predictive value for mpMRI at 3 T of 98% in the overall prostate was found.

The ability to accurately localize PCa enables the application of MRI for directing biopsies of tumour lesions, namely MR targeted biopsies (MRGB). MRGBs can be divided into three categories of approaches [23, 26]. Firstly, approaches in which registration or fusion software is employed to combine both MR and US-images. This allows an MR-defined lesion to be identified on US-images during a TRUSGB procedure. Secondly, approaches called *cognitive* tracking in which the physician performs a TRUS-biopsy using prior knowledge of the lesion as seen on MR and applying it to select the appropriate biopsy site by means of US-visualisation. These two kinds of approaches are referred to as *out of bore*. Exclusively MR based are the *in bore* approaches that acquire a pre-biopsy MR to define the targets and use MR to guide and control the procedure. This study focusses on the final approach and uses a method which has previously been described [27, 28]. In a prospective comparison with TRUSGB, this approach reduces the detection of low-risk PCa (-87.2 %) and the number of men requiring biopsy (-36.3%), while increasing the detection of intermediate/high risk PCa (17.7%) [29].

A limitation of this method is that it is rather time consuming while MR-time is scarce. Hambrock et. al [30] reported a median biopsy procedure time of 35 minutes (range, 21-75 minutes). The goal of our study is to prospectively achieve proof-of-principle of an *in bore* MRGB method that uses a real-time MR-sequence in combination with an in-room mobile touching device (MTD) to guide and control the procedure at in vivo patients. Furthermore, we will evaluate whether the proposed method can reduce the time expenses, and examine the accuracy of the procedure.

Chapter 4

Determination of the safe distance between the MR bore and an MTD through ASTM F2052-06

4.1 Introduction

Currently, the possibilities to employ a mobile touching device (MTD) into the MR room to monitor and target MR guided prostate biopsies (MRGB) are investigated. A key requirement before employment can take place is knowledge of the MR-safety of the device. This experiment will address the measurement of the magnetically induced displacement force produced by static magnetic field gradients on the MTD and the comparison of that force to the weight of the device. The goal of this experiment is to find out to what distance to the MR bore the MTD can be positioned during an MRGB without being sucked into the MRI. A secondary goal is evaluation of the MTD's functionality when positioned in a strong magnetic field.

4.2 Materials

The magnetic field in which the MTD was tested was generated by a 3 T Magnetom Skyra (Magnetom Skyra, Siemens AG, Erlangen, Germany). The MTD in question was an iPad 2 (iPad 2, Apple Inc., Cupertino, CA, USA). A custom made wooden construction holding the protractor was used to attach the MTD to the IV pole. A custom made bag from cotton fabric able to hold the MTD was suspended from the wooden construction through a string and screw-eye. In turn, the wooden construction was tie wrapped to the IV pole. Figure 4.3 provides an overview of the construction.

4.3 Method

The method in this experiment was adapted from the ASTM F2052 – 06 standard test method for measurement of magnetically induced displacement force on medical devices in the magnetic resonance environment [31]. The magnetically induced displacement force is produced when a magnetic object is exposed to the spatial gradient of a magnetic field causing the object to translate in the gradient field. This method intends to find the point in a magnetic field that produces the greatest magnetically induced displacement force on a device that is suspended from a string. Therefore, the angular deflection, α, of the string from the vertical is measured. If the device deflects less than 45°, the critical deflection angle, then the magnetically induced displacement force (F_m) is less than the force on the device due to gravity (F_g). In that case, the device will not be sucked into the MR bore. These forces are visualised in the free body diagram in figure 4.1. Note that any induced torque by de magnetic field is left out of consideration as this requires a different testing method. Furthermore, investigating the induced torque was not required for accomplishing the current research goal. The ASTM method was slightly extended for the current experiment to accommodate for research purposes. The major adaptation that was made was that a grid of multiple measure positions was chosen rather than finding the one position of maximum deflection. With this grid, information of the deflection angles on various positions in the MR room could be obtained providing a global indication of safe (MTD not drawn into the bore) and unsafe (MTD drawn into the bore) use of the MTD. Besides that, the critical deflection angle of the MTD was determined at multiple locations. Therefore, a so-called critical angle line could be determined indicating save use of the device for positions farther away from the MRI and unsafe use for positions closer by the MRI.

The MTD was positioned on varying distances from the bore not only on the centreline but lateral from that line (x-direction) as well, at -80, -40, 40 and 80 centimetres with the centreline located at 0. In the longitudinal (z-axis) direction, thus along B_0, the MTD was positioned at 10, 20, 30, 40, 50, 70, 100, and 150 cm. A measurement was considered invalid in case the MTD would touch the MR bore. This could be the case at the bore distances of 10, 20 and 30 cm considering the length of the string of ± 30 cm that suspended the MTD. To reach the desired measure positions the MR table was removed. The measurement positions are depicted in figure 4.4. The positions were marked on the floor such that multiple measurements (n=3) could be performed.

By eye-balling the obtained deflection angles of the MTD on the different positions an estimate of the location of the critical angle line could be made. Subsequently, a more precise determination of its location was done by slowly setting the deflection angle on 45°by moving the IV pole closer by of farther away from the bore. Once 45°was achieved the distance from the bore was measured.

The performance of the MTD was evaluated on observational basis.

4.4 Results

The results of this experiment are reported as specified in section 10 of the ASTM document [31] with an additional part concerning the different deflection angles at varying positions and the critical angle line. This is additional part 14. Additional part 15 addresses to the MTD's performances

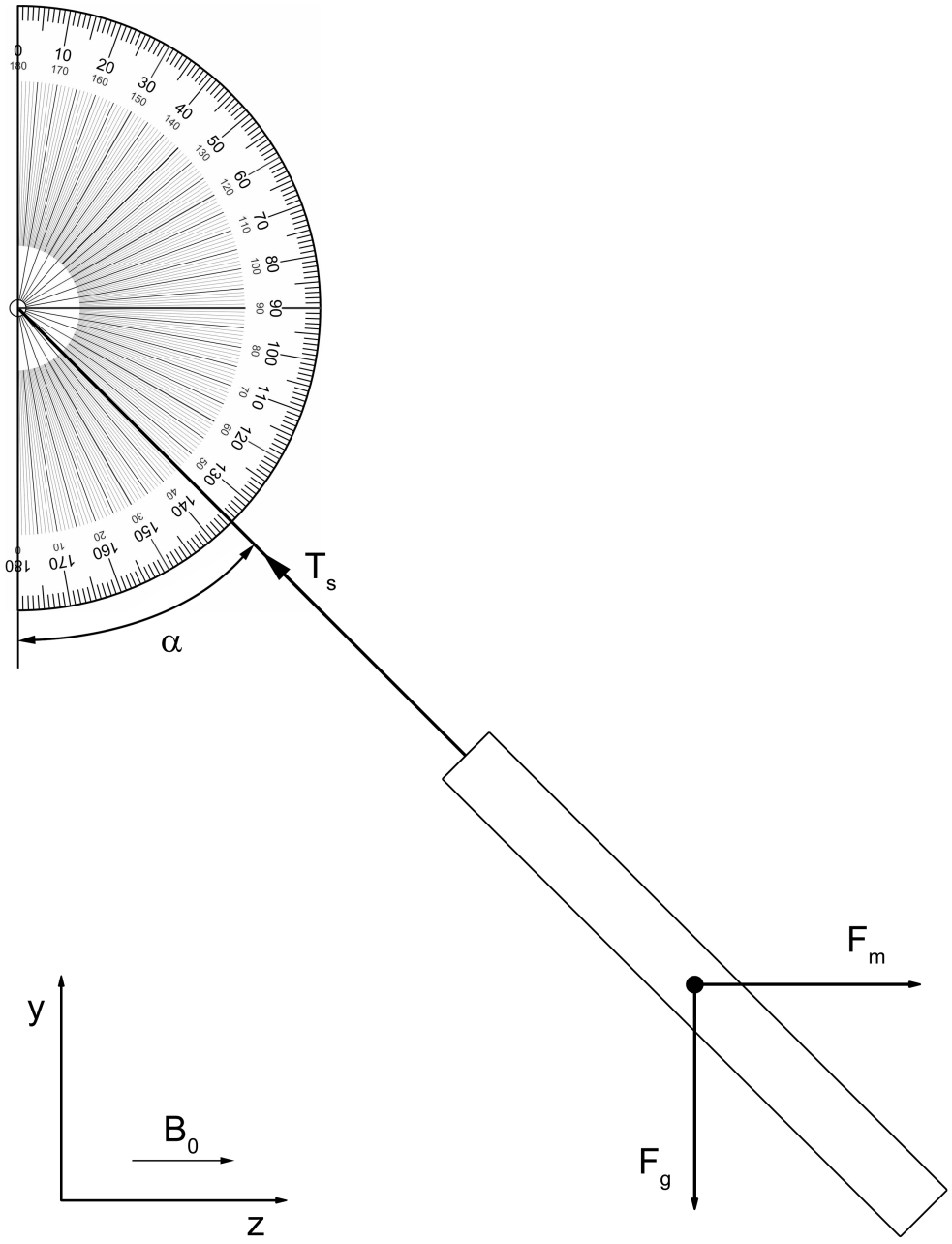

Figure 4.1: Force- or free body diagram of the MTD in the magnetic field. Where T_s =tension in string, F_m =magnetically induced displacement force due to magnetic field spatial gradient, F_g =gravitational force, and α angular deflection of string measured with protractor

in the strong magnetic field. The numbering (from 1 to 13) in this section corresponds with the numbering in section 10 in the ASTM document.

1. **Device product description**
   A frontal and lateral appearance of the MTD is depicted figure 4.2. The device characterised by a large capacitive touch screen and the round home button on the front. On the lateral side, various buttons are situated such as volume control etcetera, which are not depicted. The back of the device consists of aluminium acting as an encasement.

2. **Photograph of the configuration**
   Figure 4.3 contains a photograph of the configuration of the device as used in the experiment. It shows the MR compatible IV pole holding a custom fabricated fixture with attached protractor and the cotton bag containing the MTD. The fixture itself consists of two wooden parts: a stick and a block (behind protractor) joined together with wooden plugs. The protractor was stuck on cardboard which in turn was taped onto the wooden block. A metal screw eye was inserted through the centre of the protractor and tightened into the wood. The cotton sac with sewn string was used to hold the MTD and could be suspended from the screw eye. The cross on the sac marks centre of gravity of the MTD. The entire fixture with attachments fixed onto the IV pole using 4 tie wraps (top one not visible). Some additional tape was used to resist a final amount of movement between the pole and the configuration. Except for the screw-eye no magnetisable metals were used.

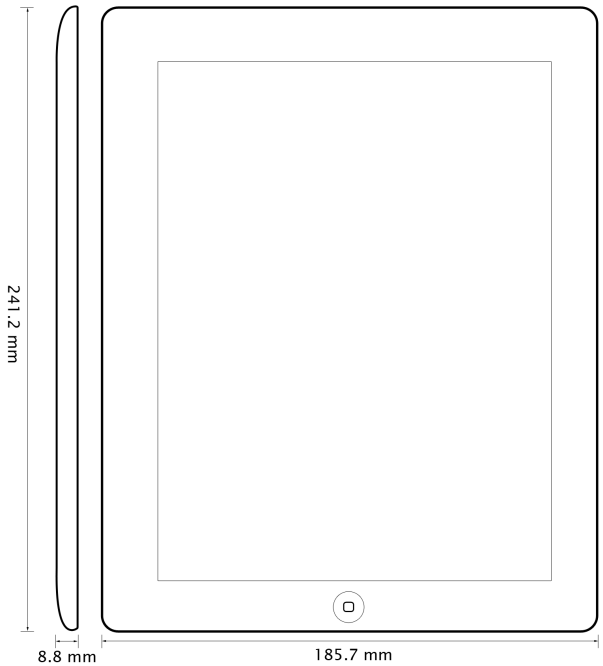

Figure 4.2: Schematic frontal and lateral representation of the MTD.

Figure 4.3: Photograph of the configuration as was applied in the experiment.

3. **Device product identification**
   - Commercial name: Apple iPad2 32GB Wi-Fi
   - Model number: A1395
   - Serial: DN6FMVYDFHY
4. **Materials of construction**
   The materials of construction of the MTD could not be retrieved.
5. **Number of specimens tested**
   Only one specimen of the MTD was tested. It was considered unnecessary to test multiple of them.

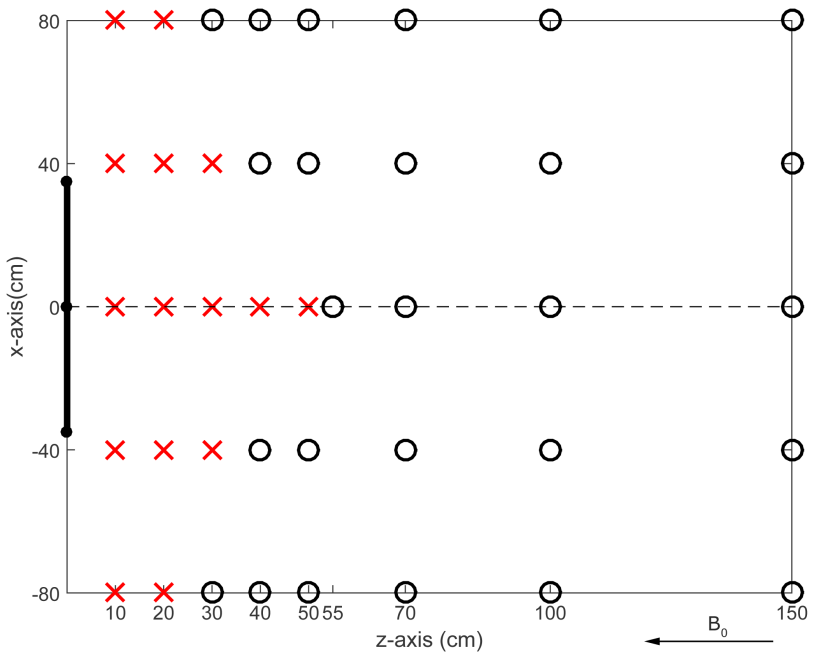

Figure 4.4: Measurement positions as viewed from above in the xz-plane. The red crosses mark the positions at which a deflection angle could not be reliably measured,while deflection angles were successfully measured at the black circles

6. **Coordinates of the test locations**

   The origin of the Cartesian coordinate system was chosen at the centreline of the MR bore at the face of the device, the edge of the bore, rather than positioning it at the isocentre of the magnet. Considering the aim of the study this was a rational choice. The MTD was positioned on different positions in the xz-plane, which were marked on the floor such that repeated measurements could be performed as accurately as possible. The y-position of the device was kept constant at a position of 124.5 cm from the floor. This distance was not chosen deliberately, but was a result of roughly hanging it at the intended height for future use. Figure 4.4 provides the defined measurement positions as viewed from above, thus in the xz-plane. Deflection angles were not successfully determined at each of the predetermined test locations. A measurement was designated unsuccessful when the MTD touched the bore during a measurement, which was the case in the z-distances of 10 and 20 cm, or when the IV pole could not be moved, thus did not fit, at the specific test location. At x = 0, the MR table connection unit prevented the MTD from being closer than 55 cm from the bore. As a result, the z=55 measurement was performed instead of the z=50 measurement.

7. **Values of |B|and |∇B|**

   All the measurements were performed within the 3 mT isoline of the magnetic field. A room plan depicting the isolines of varying field strengths is shown in figure 4.5. Further detailed information on the field strengths exerted more closely to the bore was unavailable. Therefore the value of the magnitude of the magnetic field, ||B|, was between 3 mT and 3 T during the

measurements. In turn, given the 3 mT isoline at 3168 mm form the isocentre of the magnet, the magnitude of the spatial gradient of the magnetic field, $|\nabla \mathbf{B}|$, was 0.95 T/meter.

8. **Measured deflection angles**
   Table 4.1 contains the deflection angles, α, of each measurement (n=3) at the various test locations that provided a representative measurement as marked by the black circles in figure 3. In all cases the MTD was attracted to the magnet.

9. **Mean deflection angles**
   Table 4.2 contains the mean deflection angles at each test location. These means angles are represented graphically in figure 4.6 and 4.7. The data in between the predefined test locations was interpolated.

10. **Weight of the MTD**
    The weight of the MTD, the iPad2, was 603 grams.

11. **Weight of the string and bag**
    The weight of the string and back to suspend the MTD from the test fixture was 39.5 grams.

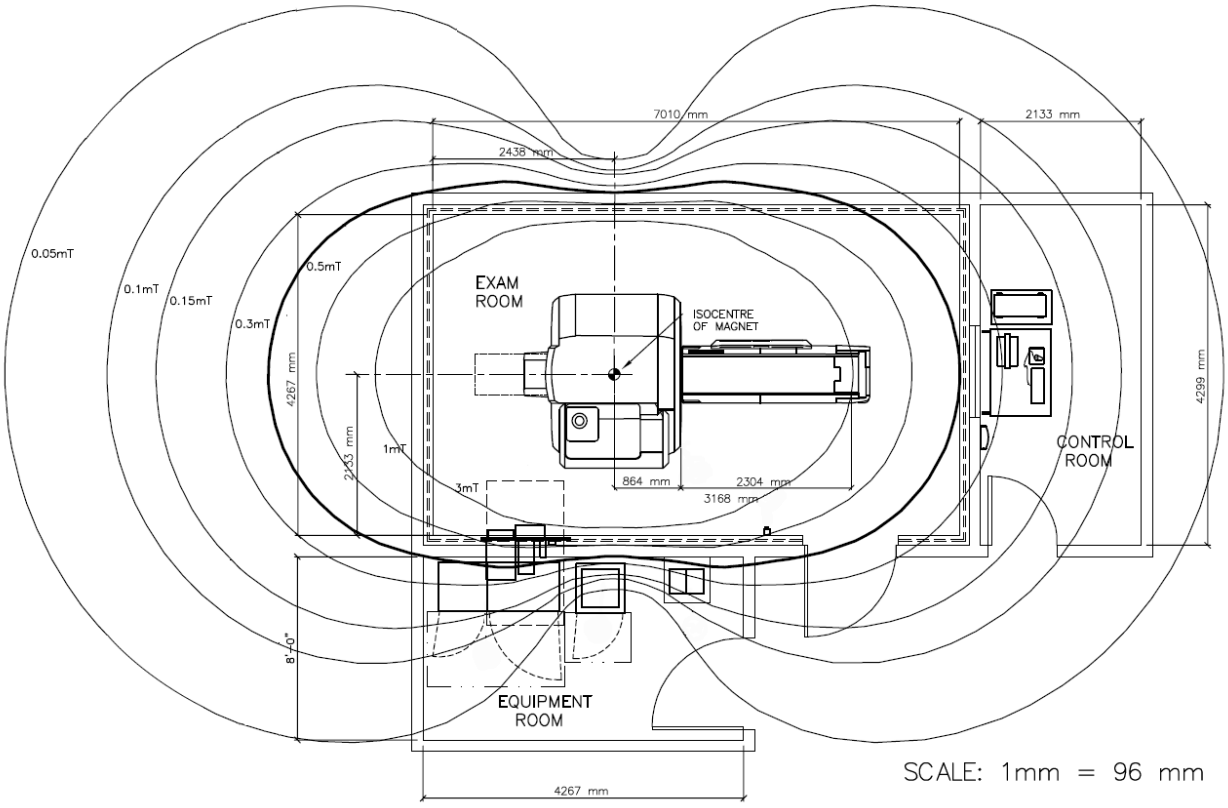

Figure 4.5: The floor plan above resembles the MRI layout and magnetic field lines at our institution except for the equipment room that is located at the opposite side. All deflection angle measurements were performed within the inner isoline of 3 mT which is situated at 3168 mm from the isocentre of the magnet, thus 2304 mm from the bore entrance.

12. **Weight of material used to constrain the MTD (test fixture)**
    The weight of the material, the test fixture, used to constrain the MTD during the test 252.2 grams

13. **Mean magnetically induced displacement force**
    The mean magnetically induced displacement force, Fm, was calculated from the measured test data for each individual position. This was done by applying the following relations which has been derived from the force diagram in figure 4.1

$$\Sigma F_z = 0 = F_m - T_s \sin(\alpha) \tag{4.1}$$

$$\Sigma F_y = 0 = T_s \cos(\alpha) - mg \tag{4.2}$$

    Solving these two equations provides :

$$F_m = mg \tan(\alpha) \tag{4.3}$$

    Where m is the mass of the device, g is the gravitational acceleration, and α is the angular deflection of the string measured with the protractor. When applying equation (4.3) on the values in table 4.2 where $m = 0.603kg$ (see part 10) and $g = 9.81\frac{kg}{s^2}$ table 4.3 is obtained.

14. **Determination of the critical isoline**
    The z-position of the critical isoline was globally localised by observing the obtained deflection angles (table 4.1). Initially, the position was determined between z = 40 and z=50 cm. As a result, the critical isoline could be determined only on x = -40 and 40. This was because at x = 0, the MTD could not be brought closer than z = 55. Another reason was that a deflection angle of 45 degrees could not be reached at x = -80 and 80 as the MTD already touched the MRI bore at lower deflection angels. The z-positions at which a deflection angle of 45 degrees was reached were determined three times at both x = -80 and x = 80. These values were averaged as well as the averages resulting from both the x-positions. See table 4.4. The critical isoline is visualised in both figure 4.6 and 4.7.

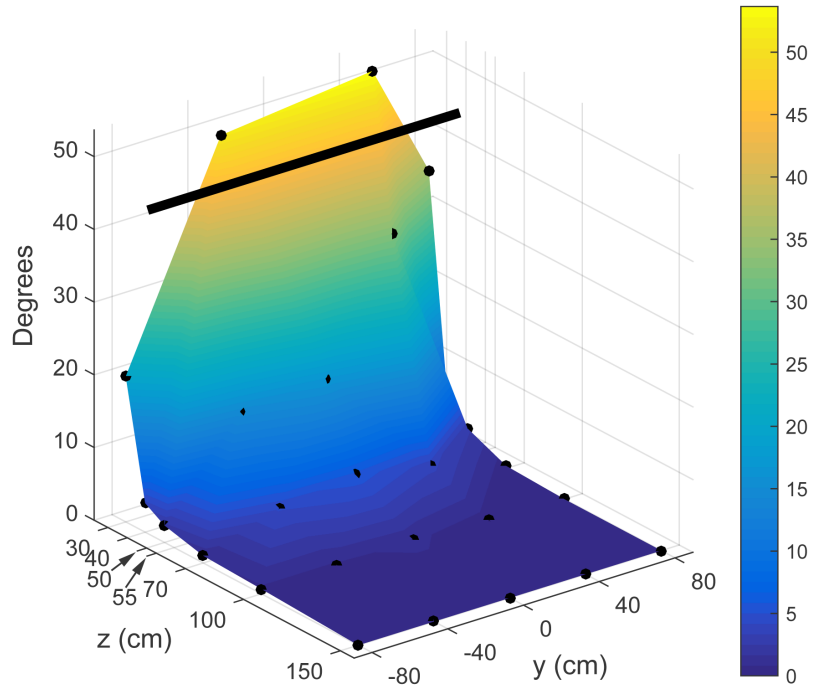

Figure 4.6: Three dimensional representation of the deflection angles in degrees at the different test locations.

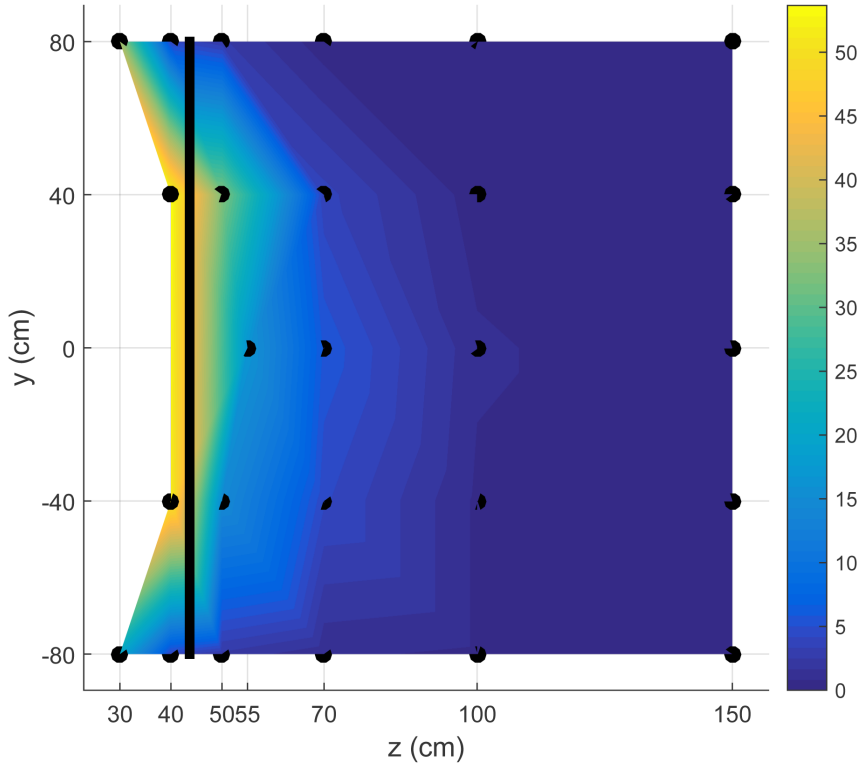

Figure 4.7: Two dimensional view from figure 4.6 The black dots represent the factual measured angles whereas the data in between was interpolated. The black line represents the critical isoline which was determined at 43.7 cm from the face of the MR bore.

Table 4.1: Measured deflection angles, α, in degrees were determined three times at each of the test locations.

z \ x	-80			-40			0			40			80		
30	19	21	20		n/a			n/a			n/a		35	35	36
40	4	4	4	51	51	52		n/a		53	54	54	4	4	5
50	2	2	3	14	14	16		n/a		34	32	32	3	3	2
55		n/a			n/a		15	20	15		n/a			n/a	
70	1	1	1	4	4	5	5	6	6	3	4	4	0	1	0
100	0	1	1	1	1	0	1	1	1	0	1	0	0	0	0
150	0	0	0	0	0	0	0	0	0	0	0	0	0	0	0

Table 4.2: Mean deflection angles at each of the test locations. Angles are in degrees.

z \ x	-80	-40	0	40	80
30	20	n/a	n/a	n/a	35.3
40	4	51.3	n/a	53.7	4.3
50	2.3	14.7	n/a	32.7	2.7
55	n/a	n/a	16.7	n/a	n/a
70	1	4.3	5.7	3.7	0.3
100	0.7	0.7	1	0.3	0
150	0	0	0	0	0

Table 4.3: Mean magnetically induced displacement force, F_m in Newton on the MTD

z \ x	-80	-40	0	40	80
30	2.2	n/a	n/a	n/a	4.2
40	0.4	7.4	n/a	8.0	0.4
50	0.2	1.5	n/a	3.8	0.3
55	n/a	n/a	1.8	n/a	n/a
70	0.1	0.4	0.6	0.4	0
100	0.1	0.1	0.1	0	0
150	0	0	0	0	0

Table 4.4: Determination of the z-position of the critical isoline. Values are in centimetres.

x-postion	45˚at z-position			Mean z-position
x = -80	45	46	43	44.7
x = 80	42	44	42	42.7
		Overall mean:		43.7

15. **Functionality of the MTD in a strong magnetic field**
    The MTD remained functioning properly when positioned in the magnetic field near the MR (<1m). However, its functions severely worsened when brought closer to the MR which caused the screen to flicker and eventually the entire device to *freeze*. This occurred at z-positions smaller than ± 30 cm. Functions returned to normal when the device was removed from the magnetic field, however in case of freezing this required a hard reset by simultaneously holding the *home* and *standby* button for 10 seconds. When holding a static position within the magnetic field the effects did not occur as fierce when moving it around in the field. This can be explained by appearing induction effects.

4.5 Discussion and conclusion

The critical isoline found during this study is at twice the distance as the line found in Kogelman's thesis, 43.7 cm versus ± 21 cm [32]. An explanation for this could be the fact that one long side of the MTD is more attracted to magnet than the other. As a result a different deflection angle can be measured at the same z-position by just turning a different side towards the bore. In this study a "worst case scenario" was chosen, thus the more attracting side was faced towards the MRI.

Two weaknesses regarding this study should be noticed. Firstly, the cotton back and string used to suspend the MTD weighted more than 1% of the MTD itself, whereas the ASTM demands it to weigh less than 1%. Therefore, a safety margin should be included when determining the safe use zone of the MTD. The second weakness of this study was the limited precision at which the test fixture was crafted and at which the IV pole could be positioned. However, the three measurements at each position showed limited variation, so this should not be considered a problem.

Finally, the fairly large discrepancy between the (z,x) = (40, -40) and (z,x) = (40, 40) should be noticed. An explanation for this could either be incorrect positioning of the IV pole due to an erroneously placed floor marker or the fact that the front face (screen) of the device is less attracted than the back side (encasement). At positions next to the centreline (x=0) the MTD was somewhat attracted in an oblique fashion, always towards the centreline. While the front face was always pointed in the negative y-direction, this could alternately cause the MTD to be attracted more when located in negative y-positions, and vice versa in positive y-positions. Of course, this only holds true when aluminium back side is more attracted than the screen side which might shield the device. However, this has not been thoroughly proven. Such a discrepancy can also be noticed between z = 30, y = -80 and z = 30, y = -80, be it to a lesser extent. The other measurements showed no discrepancies.

In conclusion, this study proved that the device will not be sucked into the MRI when used at positions that are farther away than 43.7 cm the MRI bore. For the sake of safety a margin should be included, making 50 cm a more applicable distance. Besides that it can be concluded that the MTD remains functional at that distance.

Chapter 5

Determination of the accuracy of MR guided prostate biopsies using real time MR imaging and an iPad for visualisation

5.1 Introduction

The current procedure of performing MR guided prostate biopsies is time consuming as the operator has to move between the MR room and the control room to steer the needle guide and operate the MR, respectively. Depending on the position of the lesion within the prostate and the number of lesions, a complete procedure might take up to 75 minutes [30]. A suggested solution to this drawback is the implementation of a mobile touching device (MTD) within the MR room on which real-time MR images of the procedure are visualised. In this way, the movement of the operator could be reduced to a minimum and valuable MR time could be saved.

In a previous study the MR safety aspects of the MTD in question were addressed and it was found that the device could be used safely at a distance of 50 cm from the bore. This study, however, addresses the accuracy of the proposed method by conducting a phantom experiment. The goal is to evaluate whether the target is actually hit when the needle guide is directed by using real-time MR images which are visualised on an in-room MTD. Next to the success rate, the amount of deviation between the target and the needle is examined as well as the time to target the needle guide. The outcome is applied to support the verdict whether conducting a subsequent patient study would be responsible or not.

Figure 5.1: The four phantom with the twelve CSRs still visible are depicted. Shortly after, the top layer of the phantom was moulded. The two cups on the left contain the small CSRs, the two on the right the large ones.

5.2 Materials and methods

5.2.1 Phantom

Four phantoms were made of agar (DI water, 3% w/v agarose, 0.2% w/v NaCl) and were moulded into coffee cups. In each of the cups, three raisins that represented cancer suspicious regions (CSRs) were inserted 2 cm under the rim of the cups. In this way, the raisins were positioned in an area that could be completely covered by the biopsy device as is the case with a patient's prostate. The total of twelve raisins in four 'prostates' consisted of two equal categories of size, namely, small: $\pm$ 5 mm, and large: $\pm$ 10 mm. On T2 weighted MRI, the raisins appeared as hyper intense white spots on a gray background of agar.

5.2.2 Fixture

In order to support the cups and to be able to reach the phantoms with the biopsy device, a custom poly(methyl methacrylate) (PMMA) fixture was made. The fixture raised and tilted the phantom so that is came in reach of biopsy device. See figure 5.4.

5.2.3 General set-up

Images were acquired with a wide bore (70 cm) 3 T MRI system (Magnemtom Skyra, Siemens, Erlangen, Germany). The procedure was planned using Interactive Front End (IFE) software from Siemens that was installed on a dedicated PC, the IFE PC, which was positioned in the control room. Furthermore, this PC transferred the images that were visualised on the MTD. The MTD, an iPad2 (Apple Inc., Cupertino, CA, USA) was situated in the MR room and was mounted on a MR compatible IV pole using a car kit holder. The IV pole was positioned next to the MR table at 75 cm from the bore, which was considered a convenient distance for looking at the screen. Both the aforementioned PC and the MTD were connected to the same WiFi network. In this way, it

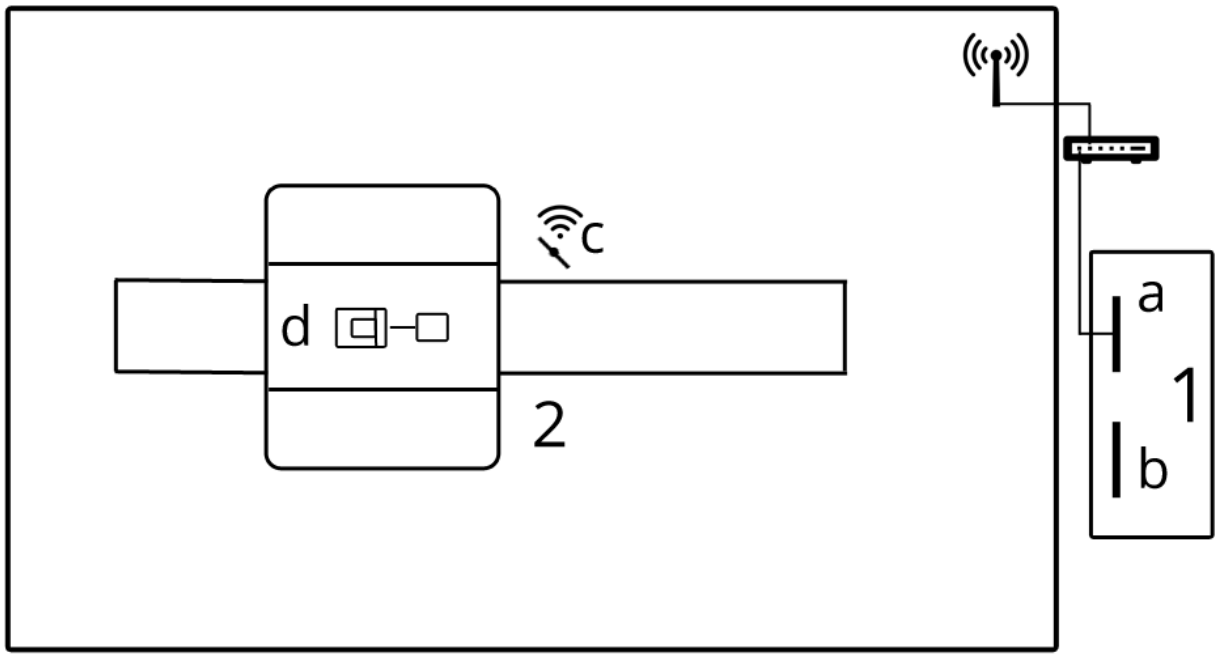

Figure 5.2: Floor plan of the general set-up during the experiment with: **(1)** the operator controlling the MR, **(2)** the operator controlling the biopsy device, **(a)** the IFE PC, **(b)** the MR computer, **(c)** the MTD mounted on the IV pole, and **(d)** the phantom and biopsy device while being imaged in MR scanner.

was possible to use remote desktop software to visualise the real-time MR images on the MTD. The phantom was placed on the dedicated fixture. A body coil was placed covering the phantom. The biopsy device, DynaTRIM, with attached needle guide (both Invivo, Gainesville, FL, USA) was positioned in front of this. Figure 5.2 gives an overview of the general set-up.

5.2.4 Procedure

Once all preparations were made, the biopsy procedure itself was performed as follows (see table 5.1 for detailed sequence parameters):

1. Subsequently to obtaining localizer images, T2 weighted MR images of the phantom were acquired and the CSRs were located.

2. The T2 images were transferred from the MR computer to the IFE PC using a build-in transfer tool that comes with IFE.

3. The slices for the real-time sequence were planned in IFE, see figure 5.3. In short this came down to defining a target and entry point, defined at the pivot of the needle guide (see appendix A), to create a trajectory. Next two slices were positioned orthogonally to each other through this trajectory. This occurred in such a fashion that one slice, the coronal slice (as defined by IFE, bottom-left in figure 5.3) visualised the left-right displacement of the needle and the other one, the sagittal (as defined by IFE, bottom-right in figure 5.3) the

up-down displacement. See appendix B for more details on slice planning in IFE.

4. The slice planning was transferred back to the MR computer using the same channel as in step 2.

5. The real-time MR sequence (BEAT-interactive real-time tip tracking (iRTTT)) for visualisation of the procedure was started. The moment that the sequence started, images were visualised on both the MR computer as well as on the IFE PC which is a build-in IFE functionality. The images were *shared* from the IFE PC with the MTD trough team viewer software (VNC viewer, RealVNC Ltd, Cambridge, UK). The BEAT sequence acquired an MR image every 240 milliseconds (ms), the refresh rate of an individual image direction was 720 ms.

6. While standing in the MR room, the visual information on the MTD was used to set the needle guide in the correct orientation, i.e. the needle guide has to be positioned across and alongside the projected trajectory in both slices. The real-time visual feedback provides an intuitive way of orientating the needle guides. A correct orientation was achieved by loosening setscrews 1 and 2 (see figure 5.3) allowing for up-down and left-right adjustment respectively.

7. True-FISP (TRUFI) images in two directions, axial and sagittal with an orientation identical to the BEAT images, were acquired to verify the orientation of the needle guide before taking the actual biopsy. The images were obtained once again when the biopsy needle was in place.

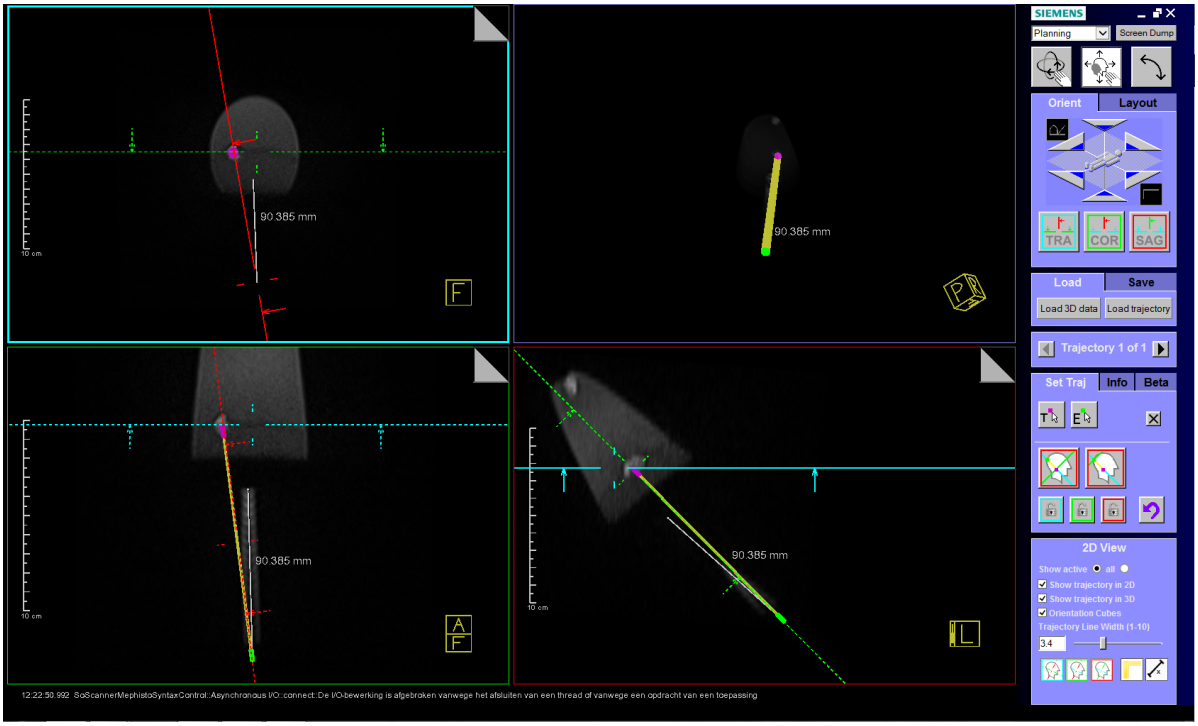

Figure 5.3: Screen capture from the IFE interface while planning MR slices. The yellow rod is the planned needle trajectory, with the entry point coloured green and the target point in purple.

In this case one set of T2 images was obtained per phantom, based on this set a planning could be made for all three CSRs within the cup. The biopsy procedure was performed by two operators: one operated the MR while the other was in the MR room to set the needle guide. Positions were switched after six CSRs were targeted, this occurred in such a manner that both operators had one phantom containing small CSRs and one containing large CSRs.

5.2.5 Data analysis

By subtracting the acquisition time from the last and first BEAT-iRTTT image, the mean time required to adjust the needle guide in the desired position was defined. In terms of accuracy two analyses were performed.

On the one hand the success rate of the method was considered, which was done by visually verifying whether the needle trajectory traversed the CSR using the post needle insertion TRUFI images. On the other hand the accuracy was expressed in the deviation of the needle from the target. Thus, the shortest distance between a point -the centre of the CSR- and a line -the needle trajectory- was calculated. The deviation was determined separately for the axial and sagittal images directions, thus the right-left deviation and the up-down deviation. Both these analyses were performed using software written in Matlab (MathWorks, Natick, MA, USA) for which only the pre needle insertion TRUFI images were employed, because the needle in the post needle insertion image is known to cause artefacts.

The written software presented the user a graphic user interface (GUI) in which both TRUFI images could be visualised. Next, the user had to manually define the centre of the CSR. The needle trajectory could be roughly defined by drawing a line between the two hyper intense borders of the needle guide. Subsequently, a build-in algorithm repositioned this line to the centreline of the needle guide corresponding with the needle trajectory. Furthermore, the line was extrapolated so that it was visible if the needle traversed the CSR and with that it was determined whether the biopsy had been successful of not. The CSR was hit by the needle in all twelve cases in both axial as well as sagittal slice direction. When both the point and the line were defined, the script automatically determined the shortest distance between these two. See appendix C for a more thorough description of the GUI.

5.2.6 Statistics

Independent samples Student's t-tests were applied in the statistical analysis. P values smaller than 0.05 were considered significant.

Table 5.1: Parameters of the applied MR sequences. T2W, T2 weighted; TSE, turbo spin echo; BEAT-iRTTT, adapted cardiac MR sequence with interactive realtime tip tracking; TRUFI, TrueFisp; TR, repetition time; TE, echo time; ST, slice thickness

Sequence	**# slices**	**TR(ms)**	**TE (ms)**	**ST (mm)**	**Aver-ages**	**Voxel size (mm)**	**Matrix**
T2W-TSE	50	13,923	87	3	1	0.75	256×256
BEAT-iRTTT	-	240.19	1.52	5	1	2.34	128×128
TRUFI	5	4.56	87	3	1	0.75	256×256

Table 5.2: Needle deviation in millimetres determined in axial and sagittal slice direction.

	Axial deviation	**Sagittal deviation**	**Operator**	**Target size**
Target 1	2.3288	0.2254	1	Large
Target 2	2.1381	1.1830	1	Large
Target 3	2.5975	0.4545	1	Large
Target 4	0.1615	0.7039	2	Small
Target 5	0.4725	1.5474	2	Small
Target 6	2.5331	1.6553	2	Small
Target 7	0.1898	1.4369	1	Small
Target 8	0.1903	2.3397	1	Small
Target 9	0.7378	1.5426	1	Small
Target 10	0.7184	1.5426	2	Large
Target 11	1.5236	0.8880	2	Large
Target 12	0.9375	1.0441	2	Large
Mean ± SD	1.211 ± 0.9603	1.2636 ± 0.6406		

5.3 Results

All twelve biopsies were successfully performed the time to target the needle guide was 01:29 ± 00:22 (mm:ss).

The deviation of the needle in each image direction as well as other characteristics are presented in5.2. The mean distance between the needle and the centre of the CSR was 1.2110 ± 0.9603 mm and 1.2636 ± 0.6401 mm in the axial and sagittal slices. Statistics (P = 0.876) revealed no significant difference of the needle deviation between the two slice directions. Per slice direction statistics was performed to test for any significant difference in deviation between the operators and the target sizes. No significant difference in deviation was found between the operators in neither the axial- (P = 0.867) nor the sagittal deviation (P = 0.606). This was also the case between the target sizes in the axial deviation (P = 0.070). However, in the sagittal deviation a significant difference was found (P = 0.035) between the target sizes.

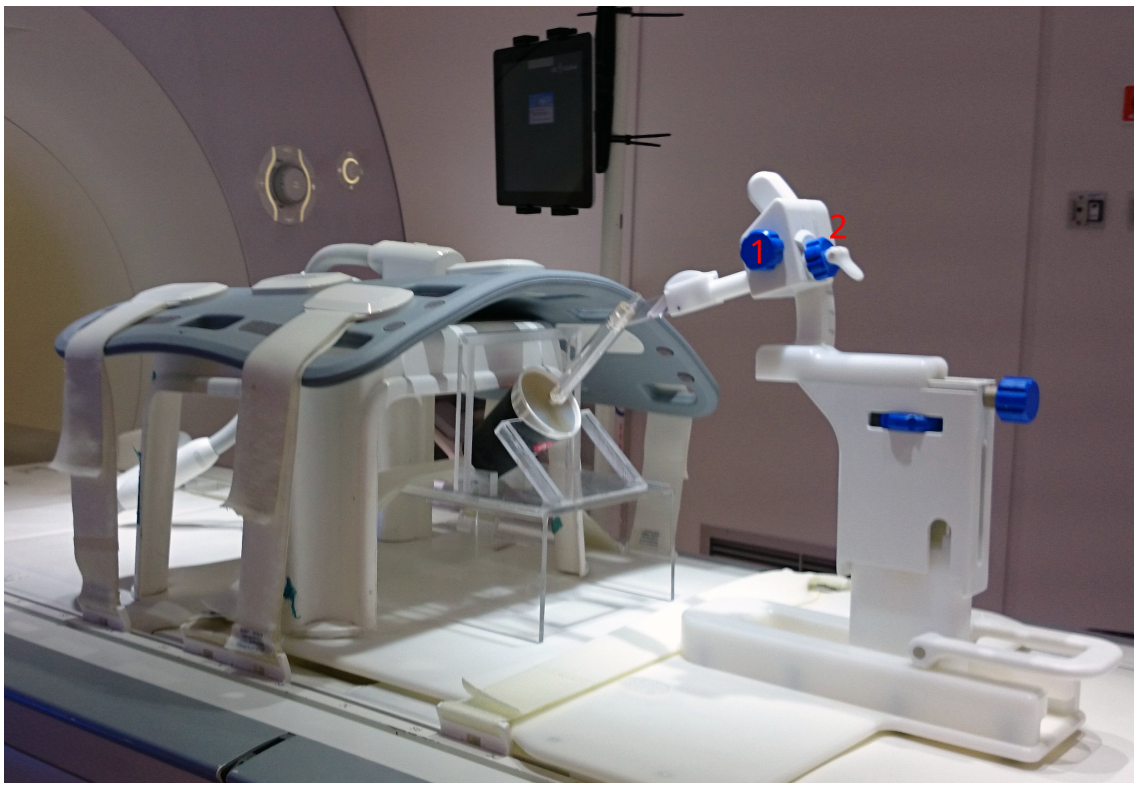

Figure 5.4: Photograph from a part of the set-up as was used during the experiment. Visible at the centre of image the PMMA fixture holding a coffee cup containing the phantom standing at the MR table just in front of the bore. At the right de biopsy device holding the needle guide is visible. At the left a step is positioned with the used body coil on top of it. The MTD mounted on the IV pole is positioned behind the MR table. Loosening setscrew 1 allows up-down movement along the arc. By loosening setscrew 2, left-right adjustment around its own axis is allowed

5.4 Discussion

The results of our study show that the proposed biopsy method is feasible as all CSRs were hit. Furthermore, we demonstrated that our method could save valuable MR time given the mean time to target the needle guide. Anastasiadis et al. [28] reported a mean number op prostate specimens per patient of 5.22 with a mean intervention time per single specimen of 9 minutes. When considering some additional time for insertion of the biopsy needle and acquisition of the TRUFI confirmation scans to the mean time to target the needle guide (01:30, mm:ss) we could easily achieve a mean intervention time per single specimen of 4 minutes, thus saving 5 minutes. In total our method could potentially save around 25 minutes.

The accuracy of the expounded biopsy method greatly depends on the accuracy at which the IFE planning has occurred as the position of the *target* and *entry* point as well as the slice orientation were defined manually. However, regarding the current state of IFE, this is the highest achievable accuracy while the alternative, i.e. automatic planning, most probably would have lead to a lower accuracy. Another factor that might have limited the accuracy is the low spatial resolution (2.34

mm) of the images that were acquired using the BEAT-iRTTT sequence. It is possible to increase the resolution of the images, yet a the expense of the refresh/frame rate of the acquisition. Despite these factors that limited the accuracy the described biopsy technique provides a clinical applicable method considering the fact that all of the measured needle deviations were within the boundaries of the artificial CSRs.

The image quality of the MR images was rather poor, even an extra bottle of water was needed to obtain a signal at all. In some cases it did affect the employed analysis method as the algorithm sometime had some difficulties in determining the exact centreline. However, a better image quality is expected when patients are scanned as more signal will be produced.

A drawback in the performed statistics is its low statistical power, especially when the differences in deviation between operators and target sizes are analysed (n = 6). However, these analyses are a minor consideration point as they do not directly support the main goal of the study.

5.5 Conclusion

By employing the described method it was possible to take accurate biopsies of targets down to 5 mm in a phantom. All targets were hit by applying the obtained alignment of the needle guide after real-time targeting and visualisation on the MTD. The targeting time was approximately 01:30 (mm:ss), which is favourable compared to the current clinical practice.

Chapter 6

Real-time MR guided prostate biopsies using a mobile touching device: study design on behalf of a patient study

6.1 Preceding work

Before the MTD was used to monitor and target the MRGB procedure, the magnetically induced displacement force produced by the static magnetic field gradients exerting on the device was measured. By applying a standardised testing method [31] a critical iso-line was defined that ensured safe use of the MTD in the MR environment at a minimum distance of 50 cm away from the bore entrance. At this distance, the device maintained position despite the present magnetic field gradient. However, to avoid damage attributable to human error, i.e. the device being accidentally pushed into the unsafe ($\leq$ 50 cm to the bore entrance) zone, it was secured to the MR table. After obtaining this knowledge, an accuracy experiment was performed in agar phantoms at which the procedure time was recorded as well. During the experiment, all targets (n=12) were successfully hit with an average deviation of 1.21 $\pm$ 0.96 and 1.26 $\pm$ 0.64 in the axial and sagittal direction respectively. The average time that was required to adjust the needle guide was 01:29 $\pm$ 00:22 (mm:ss).

6.2 Patient population

Prior to conducting the study, approval of the local Institutional Review Board and written informed consent from all patients were obtained. Twenty subsequent patients with a high suspicion of prostate cancer, i.e. an elevated serum PSA ($\geq$ 4.0 ng/mL) level and/or abnormal DRE, and a single suspicious finding (PIRADS 4 or 5) on prostate mpMRI, that have been referred to our department to undergo MRGB were prospectively recruited. Patients who, were unable to undergo MR imaging, had contra indications to MRGB, had a metallic hip implant or any other metallic implant or device, or had multiple suspicious lesions on diagnostic MRI were excluded from participation in this study. An equal number of patients who underwent MRGB at the conventional way were selected to form a matched patient cohort. The parameters used to identify matched patients included patient age, serum PSA level, number of negative previous TRUS biopsy sessions, and estimated lesion size on diagnostic mpMRI.

6.3 Real time MRGB in combination with the MTD

All MRGB procedure were performed on a 3 T clinical 70 cm wide bore MR system (Magnetom Skyra, Siemens AG, Erlangen, Germany). After that patient was positioned head first prone on the MR table, the needle guide was transrectally inserted, and standard T2W as well as DW imaging series were acquired to re-locate the CSR. The standard field of view of the T2W series was extended by a few extra slices to cover the entire needle guide as well. The acquired T2W images were transferred to a dedicated stand alone PC running planning software (Interactive Front End, Siemens). Subsequently, this software defined a needle trajectory for which the biopsy target and the turning point of the needle guide were manually identified and marked. The latter point, was experimentally defined at 9.0 cm from the tip of contrast filled compartment of the needle guide as seen on MRI. The software defined the needle trajectory in between these points. Thereupon, two MR imaging slices orthogonally oriented to each other were aligned to the established needle trajectory in such a way that these were only rotated in on plane, i.e. either transverse or sagittal adjustment. Using the software again, the planned slice positions were returned to the MR scanner and entered into a real-time MR sequence (BEAT-iRTTT). This sequence enabled acquisition of MR images with a frame rate of approximately three images per second, allowing an image update of the single scan direction once per second. After completing the slice planning, the physician entered the MR room while the technician started the real-time MR-sequence.

The acquired MR images were visualised on the planning software in real-time while the software simultaneously projected the planned needle trajectory within the same window. Furthermore, these images were visualised on a mobile touching device (MTD)(iPad 2, Apple Inc., Cupertino, CA, USA) inside the MR room that was connected to the stand alone PC outside the MR room using a remote desktop application over a WiFi connection (see figure 6.1 for the set-up). The

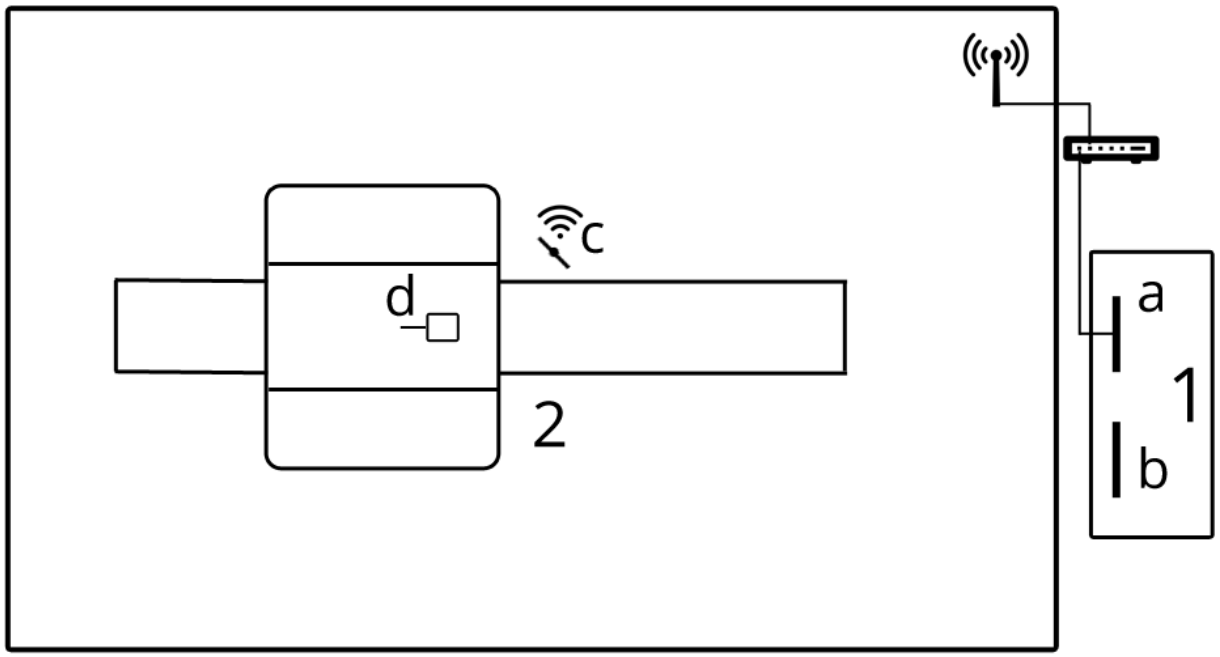

Figure 6.1: The set-up for the MRGB procedure using an MTD: **(1)** the technician controlling the MR, **(2)** the physician controlling the biopsy device, **(a)** the IFE PC, **(b)** the MR computer, **(c)** the MTD mounted on the IV pole, and **(d)** the biopsy device while in position for the biopsy procedure

MTD itself was mounted on a MR compatible IV pole using a car kit holder. This set-up provided real-time feedback to the physician facilitating him to direct the needle guide into the planned scan planes. Once the needle guide was directed into a satisfactory positions the real-time MRI sequence was stopped. Next, a confirmation scan was acquired evaluating the alignment of the needle guide according to the standard MRGB protocol. Only when the alignment was considered satisfactory on these images as well, a biopsy was taken. In case of a suboptimal alignment, further conventional adjustment was performed before a biopsy was taken.

6.4 Study endpoints

The primary outcome was the technical success rate of the real-time MRGB procedure in combination with the MTD. This success was acknowledged if the first alignment of the needle guide based on the real-time targeting procedure yielded a representative biopsy core. However, success was not acknowledged if the alignment required further adjustment after examining the confirmation scan. The secondary results were the time-to-first-biopsy and the total procedure time of the real-time MRGB protocol. The time between the final diagnostic MRI at the start of the protocol and the first confirmation scan of the first biopsy is defined as the time-to-first-biopsy, while the time of the first MR scan to the final MR scan of the MRGB procedure is specified as the total procedure time. The time-to-first-biopsy and total procedure time required for the real-time and conventional MRGB

prodcedure were statistically compared using an independent samples Student's t-test considering P values smaller than 0.05 significant.

Part III

High field ex vivo MRI to predict positive surgical margins in tumour resection specimens

Chapter 7

Ex vivo 7 T MR imaging to predict positive surgical margins in radical prostatectomy specimens

Jan Heidkamp[1], Martijn Hoogenboom[1], Iringo E. Kovacs[2], Andor Veltien[1], Arie Maat[2], J.P. Michiel Sedelaar[3], Christina A. Hulsbergen-van de Kaa[2], and Jurgen J. Fütterer[1]

[1]Department of Radiology and Nuclear Medicine, Radboudumc, Nijmegen, the Netherlands

[2]Department of Pathology, Radboudumc, Nijmegen, the Netherlands

[3]Department of Urology, Radboudumc, Nijmegen, the Netherlands

Abstract

Context: Like any other cancer treatment the success of radical prostatectomy (RP) depends on complete resection of the tumour with sufficient margins. Incomplete resection leaves the patient with positive surgical margin(s) (PSM) which is considered an adverse outcome. A potential solution could be ex vivo MRI to localize PSM providing the surgeon immediate feedback on the surgical results while the patient is still on the operation table. This technique could direct secondary additional treatment which in turn could improve patient outcome.

Objective: We investigated the performance of 7 T ex vivo MRI to predict PSM in RP specimens with histopathological examination (HPE) as the reference standard.

Method: Patients (n=12) who had biopsy proven PCa and a diagnostic multi parametric MRI prior to RP were included. After RP, the prostates were scanned in a 7 T MRI scanner using T2 weighted (T2W) and diffusion weighted (DW) sequences. Subsequently, the images were radiologically evaluated for tumour and margin status. Presence of PSM was graded on a five-point scale for the T2W and DW images separately. The assigned scores on T2W and DW images were statistically compared using an independent samples Student's t-test. The specimens were totally included, and tumour and margin status were annotated by HPE as well. Tumours that could be identified on both ex vivo MRI and histopathological slides were considered a match.

Results: A set (n=16) matching tumours was established out of the tumour that were found by ex vivo MRI (n=19) and those found by HPE (n=35). Within this set, HPE had identified four lesions with a PSM, but these were annotated as negative surgical margin (NSM) by ex vivo MRI. Furthermore, by ex vivo MRI nine of twelve NSM annotated by HPE were identified. A sensitivity of 0, and a specificity 0.75 were found respectively.

Conclusion: 7 T ex vivo MRI has failed to demonstrate the ability to predict PSM in fresh RP specimens as it showed a poor performance compared to the reference standard HPE. This is mainly attributable to the methodological limitations that were present.

Key words: • Prostate cancer • Radical prostatectomy • Positive surgical margins • Ex vivo MRI

7.1 Introduction

Radical prostatectomy (RP) is the recommended treatment with curative intent in patients with low- and intermediate risk localized prostate cancer (PCa) (cT1a - T2b and Gleason score 6-7 and PSA $\leq$20) and a life expectancy of more than 10 years [16]. Among the different methods of RP -retropubic (RRP), laparoscopic (LRP), and robot assisted (RALP)- the latter has become the dominant surgical approach as more than 75% of RPs are performed that way [33]. Like any other cancer surgery, the success of this treatment relies on complete surgical extirpation of the tumour with sufficient margins. At examination of the haematoxylin and eosin (HE) stained sections, tumour that extends to the inked surface of the prostatectomy specimen which the surgeon has cut across is defined as a positive surgical margin (PSM) and is considered an adverse patient outcome [34–36]. In addition, PSMs are associated with an increased risk of biochemical recurrence (BCR) and local disease recurrence as well as the need for secondary cancer treatment [35]. Although the risks of PSM are generally recognized, they have been reported in 15% of patients undergoing robot assisted RP [37].

The results of histopathological analysis of the specimen are not instantly available. Until then, both the surgeon and patient can not be fully certain of the success of the procedure. We hypothesize that the information obtained from an ex vivo MRI to evaluate for PSMs in the RP specimen immediately after resection while the patient is still on the operation table, can be of value for both the patient and the surgeon. The rationale is that the results of this method could be applied to direct extended resection or adjuvant radiation therapy. In turn, this might improve patient outcome. In our study, we investigated the possibilities of the application of high field MRI to predict PSM in fresh RP specimens and compared its performance with HPE as the reference standard. To our knowledge this is the first study that employs high field ex vivo MRI to predict PSM in RP specimens.

7.2 Method

7.2.1 Study population

Prior to conducting our study, approval of the Radboudumc Institutional Review Board and written informed consent from all patients were obtained. Patients who had biopsy proven prostate cancer as well as a diagnostic 3 T multi parametric MRI (mpMRI) examination, including T2 weighted (T2W), diffusion weighted (DW), and dynamic contrast enhanced (DCE) imaging, prior to undergoing RRP or RALP could be included. The time between the mpMRI and RP had to be no longer than four months.

7.2.2 Preparation of prostate specimen

Immediately after surgical resection, the entire intact prostate specimen was brought to the pathology laboratory. The specimen was weighted, inked and its dimensions were measured. A saline filled tube serving as orientation and fixation was inserted in the urethra. Hereafter, it was positioned in a custom made container (the PathoBox) manufactured in MR safe poly(methyl methacrylate) (PMMA) in which a layer of paraffin was moulded on which the specimen could be pinned down using wooden pins. The container was designed to fit into a glass box. Six saline filled rods, three on each sides of the container alongside the specimen and opposite to each other, provided reference for both pathological slicing and MR imaging. The fresh prostate was positioned and pinned down on the paraffin aspiring for an identical orientation of both the ex vivo MR images and the pathology slices. Furthermore, the specimen was so positioned that the ex vivo images could be acquired perpendicular to the rectal wall enabling a matching orientation with the in vivo MR.

7.2.3 Ex vivo MRI

The enclosing glass box was filled with perfluoropolyether (PFPE)(Galden, Solvay Solexis, Thorofare NJ, USA). Magnetic susceptibility artefacts caused by the air tissue transition were eliminated by inundating the entire specimen with Galden that does not emit MR signal. Next, the box containing the prostate was positioned in a 7 T horizontal 154 mm wide bore MR system (ClinScan 70/20, Bruker Corporation, Billererica, MA, USA), interfaced to a Siemens console (Syngo MR B15, Siemens Healthcare GmbH, Erlangen, Germany). Axial T2W and DW images, including b-values of 0-100-500-1000 s/mm^2, were acquired and aligned to the opposing rods visible on the localizer images. Furthermore, a set of sagittal T2W images was obtained and apparent diffusion coefficient (ADC) maps were calculated from the DW images using the standard ADC post processing available in Syngo BV15. The number of contiguous slices was chosen to cover the entire prostate, the repetition time was set as low as possible while maintaining T2 weighting. For further details on the sequence parameters see table 7.1. The scan protocol was optimised in one prostate specimen not included in this study.

7.2.4 Histopathological processing

Following ex vivo imaging, the Galden was poured of and the prostate was returned to the pathology laboratory for formalin fixation and further processing. After fixation, the specimen was completely included by accurately cutting it in 4 mm thick slices at which the six rods facilitated the alignment with the imaging. The 4 mm macro slides were paraffin embedded and HE stained preceding to slicing them in to 4 μm sections. Under microscopic guidance, the pathologist (C.A.H.K., 23 years experience) annotated PCa by hand using a fineliner and subsequently digitalised the slides by a flatbed scanner at 300 dpi. Furthermore, the Gleason score, extra prostatic extension (EPE),

Table 7.1: Parameters of the applied MR sequences. T2W, T2 weighted; TSE, turbo spin echo; DWI, diffusion weighted imaging; HASTE, Half-Fourier acquisition single shot turbo spin echo; TR, repetition time; TE, echo time; ST, slice thickness

Sequence	# slices	TR (ms)	TE (ms)	ST (mm)	Averages	Voxel size (mm)	Matrix	Scan time (mm:ss)
T2W-TSE	26	4800	56	2	1	0.13	512×512	05:12
DWI-HASTE	26	2000	44	2	4	0.51	128×96	4×05:12

seminal vesicle invasion, surgical margins status and length, tumour dimensions in three directions or diameter, and the pathological stage were reported.

7.2.5 Radiological assessment

Preceding the assessment of the ex vivo data, the radiologist (J.J.F., 7 years experience) was provided with the in vivo mpMRI images disengaged from any previous results which were re-evaluated which helped identifying PCa in the ex vivo MRI. In this way, a potential bias caused by the radiologist's inexperience with ex vivo MR images was avoided. The positions of the identified PCa were manually annotated on a 27 sector scheme of the prostate [38] enabling correlation of both the radiological and histopathological findings. The reader graded his confidence that a lesion contained a PSM on a five-point scale: Grade 1 indicated definitely no PSM present; 2, probably no PSM; 3, PSM possible; 4, PSM probable; and 5, PSM definitely present. Grades were assigned to the lesions for the T2 and DWI series separately.

7.2.6 Data analysis & statistics

An independent observer correlated each tumour annotated by the radiologist with a tumour annotated by the pathologist. This was done by cognitively fusing both images using landmarks such as the urethra, benign prostatic hyperplasia (BPH) nodules, and the tumour itself. Furthermore, the shape of the entire prostate as well as the shapes of the peripheral and transition zone were employed for the fusion. Tumours that could be identified on both MRI and histopathological slides counted as a match. The selection of matching tumours was applied to compare ex vivo MRI to histopathological examination in assessing PSM. The PSM probability scores assigned to lesions on T2 were statistically compared with the scores based on DWI using a Mann Whitney U-test considering P values smaller than 0.05 significant.

7.3 Results

In total, 12 patients (average age = 62 ± 5 years) were included. These patients had prostate specific antigen (PSA) values of 4.2-19.4 ng/ml (median = 8.7). After mpMRI, all patients successfully underwent RP, the time in between was 1-4 months (median = 3). Further clinical characteristics are listed in table 7.4. The number of 26 MR slides to cover the entire RP specimen was sufficient in almost every case, except for one transversal T2W series that required 30 slides and three sagittal T2W series of which one required 33 and two of them 30. Obviously, the TR and scanning time were adjusted accordingly.

In twelve fully sectioned RP specimens, with TNM stadium pT2c (n =10) and pT3a (n = 2), the pathologist annotated 35 PCa lesions. Of these lesions, five were assigned a Gleason score of 5, 18 a score of 6, ten a score of 7 and two were Gleason 8. Based on the provided tumour dimensions or diameter, the volumes ranged from 34-24,000 (median = 576) mm^3. EPE of 0.6 mm and 0.8 mm was reported in two lesions, PSMs with length 2-10 mm were reported in five lesions, and seminal vesicle invasion was not detected in any of the specimens. Additional pathological characteristics are reported in table 7.4.

In turn, the radiologist reported 19 lesions, 16 of them could be matched with an annotated lesion on the histopathological slides, while 3 of them could not as histopathology did not annotate tumour at those positions. So in terms of detection, 16 of the 35 (46%) lesions, including the five lesions with PSM, reported by the pathologist could be discovered on ex vivo MRI, yet 19 (54%) were missed. The characteristics of the found and missed lesions are described in table 7.2. The confidence grades of PSM of the 16 matching lesions for the T2W and DWI series showed no statistically significant difference (Mann-Whitney U = 128, n_1=n_2 = 16, P = 1.00). Of the 16 matching lesions, 3 had a PSM on ex vivo MRI, yet, these were issued negative surgical margins (NSM) by HPE. Likewise, the radiologist issued all four of the PSMs determined by HPE as NSM. An example is given in figure 7.1. An example of a corresponding diagnosis of NSM is given in figure 7.2. The data in the contingency table (table 7.3) resulted in a sensitivity of 0 and a specificity of 0.75. The table also contains the averages of the confidence grades the were given to a lesion classified for each contingency.

Table 7.2: Characteristics tumours by ex vivo MRI found and missed by ex vivo MRI. Number in parentheses are percentages.

Characteristic	**Found tumours**	**Missed tumours**
Gleason score ≤ 6	9(56)	14(74)
Volume < 1000 mm^3	5(31)	15(79)

Table 7.3: Performance of ex vivo MRI to detect PSM versus HPE. The numbers in the parentheses represent the average confidence grade that was assigned to each contingency with the first number the score assigned based on the T2W images and the second number based on the DW images.

	PSM present in HPE	PSM absent in HSE	
PSM present in MRI	0	3 (3.67, 3.67)	3
PSM absent in MRI	4 (2.00, 1.85)	9 (1.78, 1.89)	13
	4	12	16

Table 7.4: Clinical and pathological characteristics of the 12 patients. [a] Average value ± standard deviation. [b] Median value, with range in parentheses.

Characteristic	**Value**
Clinical characteristics:	
Age (y)	62 ± 5[a]
Preoperative PSA (ng/ml)	8.7 (4.2-19.4)[b]
Surgical technique:	
RRP	5
LARP	7
Time in vivo MRI to RP (months)	3(1-4)[b]
Highest Gleason score:	
Gleason 3 + 3	5
Gleason 3 + 4	5
Gleason 3 + 5	2
Clinical stage:	
cT1c	5
cT2a	2
cT2c	2
cT3a	3
Pathological characteristics:	
Volume (mm^3)	576 (34 - 24,000)[b]
Highest Gleason score:	
Gleason 2 + 3	1
Gleason 3 + 2	4
Gleason 3 + 3	18
Gleason 3 + 4	5
Gleason 4 + 3	5
Gleason 4 + 4	2
Pathological stage:	
pT2c	4
pT2c + R1	5
pT3a	2
EPE (mm)	0.6 and 0.8
PSM (mm)	5 (2-10) [b]

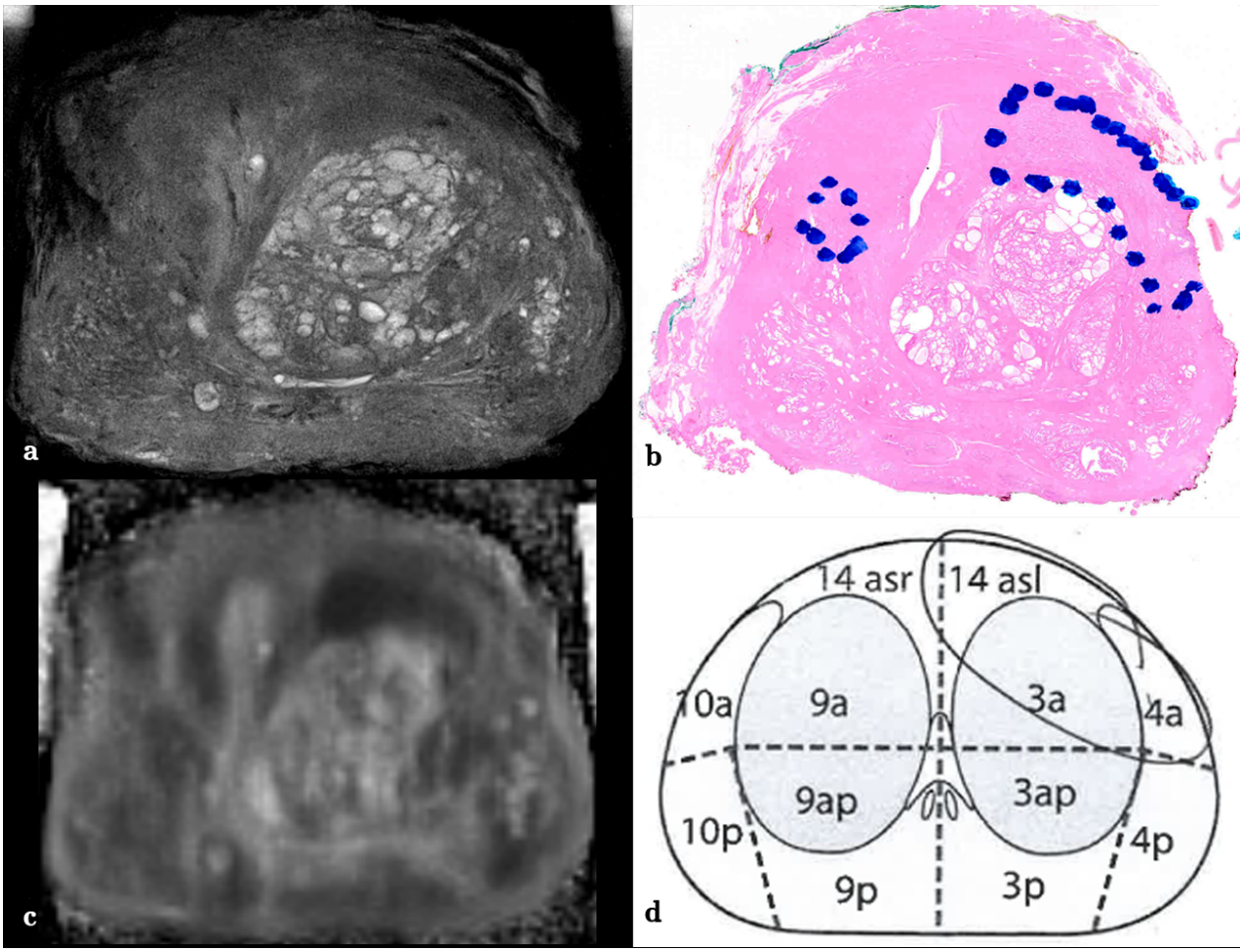

Figure 7.1: For a 62-year-old patient, **(a)**, the ex vivo T2W images, showing a large centrally situated BPH nodule, and a PCa region situated ventrally and laterally left which is only moderately visible; **(b)**, approximately corresponding histopathology slices showing the two separate lesions. Everything marked as a dotted line is cancer; **(c)**, ADC map; and **(d)** annotation by the radiologist. The lesion was issued as PSM by pathologist, but as NSM by radiologist. The figure shows a moderate match of the PCa region in the peripheral zone on the left (Gleason 4+3 = 7; volume, 6,336 mm^3) between MRI and histopathology. The lesion (Gleason 3+4 = 7; volume, 6,300), from which only a small part is annotated on this histopathology slice, on the right was not be on MRI. A fair correspondence in delineation exists between MRI and histopathology. The ADC image shows values that are smaller in the regions of cancer than in the regions of normal tissue, and better contrast between the tissues compared to the T2W image. The interruption of the dotted line on histopathology indicates the PSM of 2 mm, which was missed on MRI.

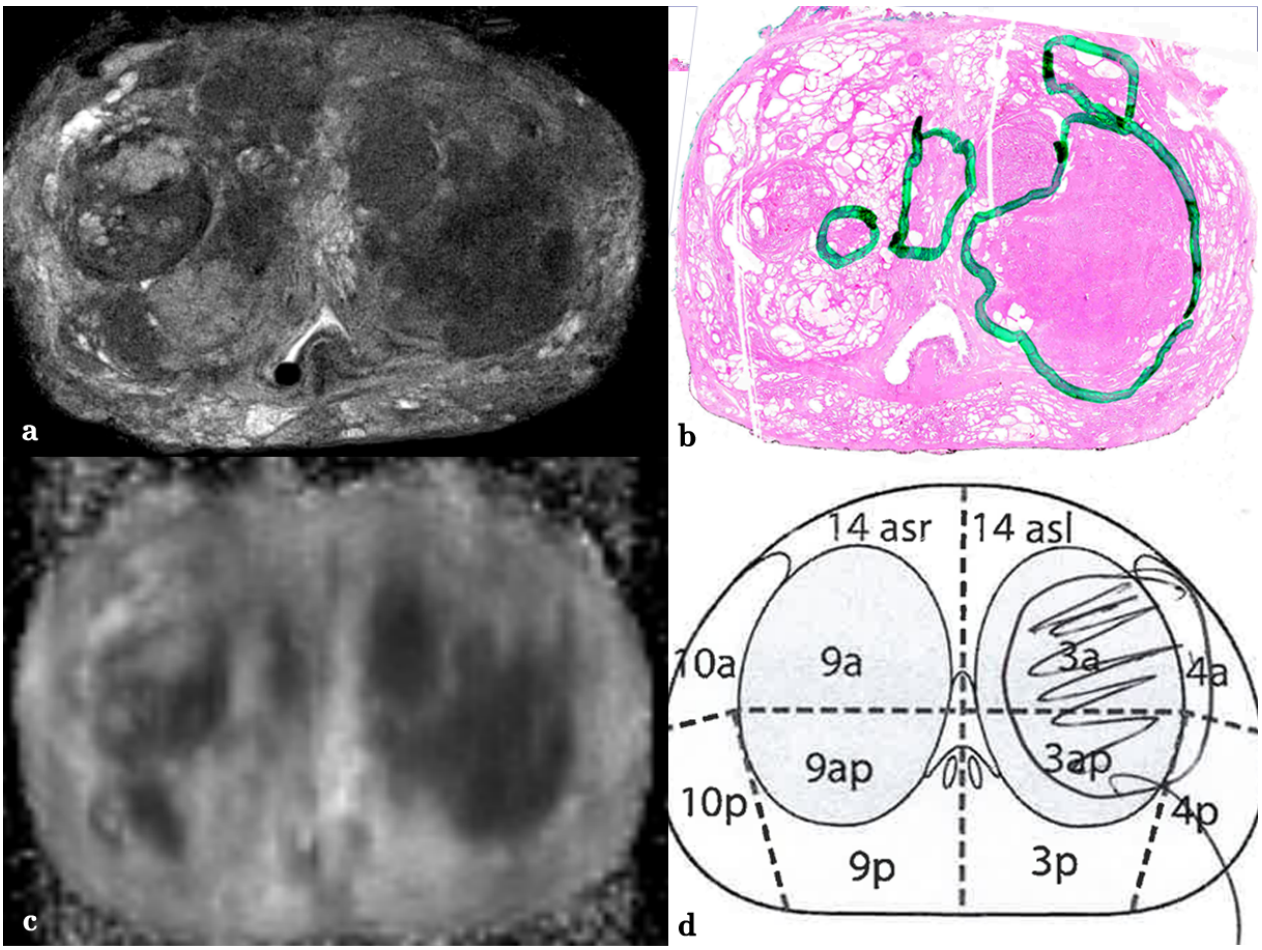

Figure 7.2: For a 67-year-old patient, **(a)**, the ex vivo T2W images, showing a low signal intensity lesion in the left transition zone suggestive of PCa.; **(b)**, approximately corresponding histopathology slices. Everything marked as solid line is cancer; **(c)**, ADC map; and **(d)** annotation by the radiologist. The figure demonstrates that the position of the PCa (Gleason 3+2 = 5; volume, 15,000 mm^3) could be matched on MRI and histopathology with a corresponding evaluation (NSM). Furthermore, the delineation of the cancer in both modalities fairly corresponds with each other, except for some small sprouts of tumour that were missed on the MRI. The ADC values are smaller in the regions of cancer than in the regions of normal tissue. Moreover, the position of a distinctive BPH nodule on the right and the urethra corresponds well on both modalities.

7.4 Discussion

While the resulting specificity of ex vivo MRI to predict PSM is reasonable, the sensitivity is considerably poor. The former is probably a result of a bias caused by more centrally situated lesions as these were usually issued negative with minor doubt, which is reflected on the low grades (average: T2, 1.78; DW, 1.89) that were assigned to the true negatives. Similarly, more doubt was present in the false negatives which were assigned an average grade of 2.00 on T2 and 1.85 on DW. The total of 13 NSMs assigned on MRI was graded with an average of 1.85 on both sequences. On the other hand, the poor sensitivity could be explained by the fact that with RP the prostate is removed using only minimal surgical margins. In addition, both the tumour and the Galden poured

around the specimen emit low intensity signal, resulting in limited contrast. As a result of these impediments, the minimally dimensioned margins of lesions situated at the edges were more difficult to evaluate. In our study this lead to an underestimation of PSM probably caused by the reader that was reserved with assigning PSM when in doubt. The uncertainty is perceived in the gradings of the PSMs that were reported on MRI (average: 3.67 for both sequences). Making directed intra operative frozen sections of these equivocal areas could be a solution to achieve a better diagnostic performance.

The aforementioned limitation in image contrast could be avoided by somehow giving the fluid a higher signal intensity while still avoiding susceptibility artefacts. This would improve the visibility of the tumour compared to the enclosing fluid. Moreover, this would facilitate the detection of margins by letting these appear as a narrow band of intermediate intensity in between. Substituting Galden with a copper(II)sulphate solution could be an option to increase the signal intensity. The concentration of this solution is crucial for the intensity and should be subject of further research.

The number of lesions (19 out of 35) that was missed on ex vivo MRI is subject of discussion. The cause of missed lesions can be partially explained by the fair amount that had either a volume of less than 1000 mm^3 (79%) or a Gleason score equal or less than 6 (74%), versus 31% and 54% respectively among the found lesions. Previous studies have demonstrated that these cancers are difficult to detect by 3 T mpMRI [39, 40]. However, when considering the relatively high in-plane resolution of the ex vivo MRI (0.13 mm) compared to the in vivo MRI (0.40 mm), it is quite likely that the reader was biased as a result of the in vivo MRI. Consequently, we assume that the reader did not look for lesions on the ex vivo MRI in regions other than where lesions were detected on the in vivo MRI.

Recently, other institutions have employed ex vivo MRI of RP specimens to improve the registration of histopathological images with in vivo MRI by using ex vivo MRI as an intermediate modality to compensate for tissue distortion due to surgical resection and fixation [41–43]. One study, conducted by Fan et al. [44], evaluated the feasibility of correlating 9.4 T MRI findings with standard prostate histopathology and showed a proper correlation between the two modalities.

Recent research has demonstrated promising results in reducing PSM by applying systematic neuro vascular intra operative frozen section (IFS) examination to direct nerve sparing RP [45,46]. In case a PSM was found, secondary additional resection was performed converting approximately 90% of PSM into NSM. A similar workflow could be achievable by applying the method we presented with no restrictions to the posterolateral side as potential PSM. Compared to IFS, our method would be more suitable for evaluating multiple potential sides of PSM at once as we were able to map the entire prostate in about half an hour added by a few minutes for radiological evaluation. In contrast, the aforementioned studies only examined both posterolateral margins by IFS which took about 30-35 minutes, adding more margins for evaluation would drastically increase the operation time. While secondary additional resection at the posterolateral sides has proven to be possible, the feasibility for other sides of the prostate is limited given the close proximity of vital structures.

For instance, performing secondary additional resection in the apex (accounting for one-third of PSM [34]) would be infeasible given the proximity of the dorsal venous complex, erectile nerves, rectum, and sphincter.

The major strength of our method is the possibility to facilitate radiation therapy after resection of the prostate. Once the PSM are identified by ex vivo MRI, brachytherapy seeds could be specifically positioned in the residual cancer area, from a logistic point of view HDR brachytherapy would be most suitable. Moreover, implanting the seeds during the RP procedure saves the patient from a separate implantation procedure. Furthermore, intra operative radiotherapy (IORT) administered as a single high fraction of radiation following RP, as described by Saracino et al. [47], could benefit from knowledge of the location of PSM because it would allow even more accurate irradiation while reducing irradiation of the entire prostate bed. Likewise, precise localization of PSM could enable more accurate repositioning of the patient for each fraction of postoperative external beam radiation by intra operative positioning of gold markers ensuring more accurate irradiation and reducing side effects.

A final remark should be made considering the study design. The design tries to answer two chronological questions instead of one, namely a) whether it is feasible to visualise and localise PCa and accompanying resection margin with high field MRI, and b), as our study intended to answer, whether it is feasible to diagnose PSM using the same modality. Answering the second question is difficult since it is hard to determine whether the results of the current study are attributable to the intrinsic inability of high field MRI to visualise PSM or the inability to employ high field MRI as a tool to diagnose PSM. A very important factor that could not be quantified is the inexperience of the radiologist to evaluate MRI images of ex vivo prostates. Future research should be performed that should especially focus on MR characteristics of PCa and resection margins for improved identification. The ex vivo MR images should be spatially correlated with the histopathological slides instead of examining them blindly. Subsequently, the ex vivo MRI should be evaluated for the recognition of tumour as annotated on the histopathological slides in an unblinded fashion, possibly by both the radiologist and pathologist together.

7.5 Conclusion

In conclusion, our study demonstrates that 7 T ex vivo MRI is not able to predict PSM in fresh RP specimens as it showed a poor performance compared to the reference standard HPE. However, the poor performance can be attributed to the methodological limitations that were present.

Chapter 8

Conclusions

The MTD can be introduced into the magnetic field that is prevalent in the MR room as long as the device is kept at a minimum distance of 43.7 centimetres from the bore entrance of the MRI. Adding a safety margin 50 centimetres is a more applicable distance. Furthermore, the MTD maintains it functionalities at that distance.

By applying the described method for real-time MR guided prostate biopsies using a MTD it is possible to successfully target artificial CSRs with a high accuracy. Morover, it enables needle guide targeting within a favourable time (mean = 01:30, mm:ss) compared to the current clinical practice.

Based on the aforementioned statements it can be concluded that the conduction of a subsequent patient study would be responsible.

High field (7 T) MRI is not able to predict positive surgical margins in fresh radical prostatectomy specimens as it showed poor performance compared with histopathological examination as the reference standard. However, conducting future research would be legitimate given the methodological limitations that attributed to the poor performance.

Bibliography

[1] M. E. Chen, D. A. Johnston, K. Tang, R. J. Babaian, and P. Troncoso, "Detailed mapping of prostate carcinoma foci: biopsy strategy implications." *Cancer*, vol. 89, no. 8, pp. 1800–1809, Oct 2000.

[2] Integraal Kankercenterum Nederland (IKNL), *Retrived from: www.cijfersoverkanker.nl*, Accessed on 15/09/2015.

[3] Centraal Bureau voor de Statistiek (CBS), *Retrived from: www.cbs.nl*, Accessed on 15/09/2015.

[4] L. A. L. M. Kiemeney, J. Meulepas, S. Rodenhuis, L. van de Poll-Franse, H. Karim-Kos, K. Aben, J. Coebergh, J. Hendriks, and S. Tax, "Kanker in Nederland tot 2020: trends en prognoses," *Signaleringcommissie Kanker van KWF Kankerbestrijding, in samenwerking met de Vereniging van Integrale Kankercentra (VIKC)*, 2011.

[5] P. Kantoff, M. Taplin, and J. Smith, "Clinical presentation and diagnosis of prostate cancer." *In: UpToDate*, M.E. Ross (Ed), UpToDate, Waltham, MA, 2014.

[6] J. O. Barentsz, M. R. Engelbrecht, J. A. Witjes, J. J. de la Rosette, and M. van der Graaf, "MR imaging of the male pelvis." *Eur Radiol*, vol. 9, no. 9, pp. 1722–1736, 1999. [Online]. Available: http://dx.doi.org/10.1007/s003300050916

[7] D. S. Smith and W. J. Catalona, "Interexaminer variability of digital rectal examination in detecting prostate cancer." *Urology*, vol. 45, no. 1, pp. 70–74, Jan 1995.

[8] C. M. A. Hoeks, M. G. Schouten, J. G. R. Bomers, S. P. Hoogendoorn, C. A. Hulsbergen-van de Kaa, T. Hambrock, H. Vergunst, J. P. M. Sedelaar, J. J. Fütterer, and J. O. Barentsz, "Three-tesla magnetic resonance-guided prostate biopsy in men with increased prostate-specific antigen and repeated, negative, random, systematic, transrectal ultrasound biopsies: detection of clinically significant prostate cancers." *Eur Urol*, vol. 62, no. 5, pp. 902–909, Nov 2012. [Online]. Available: http://dx.doi.org/10.1016/j.eururo.2012.01.047

[9] B. Djavan, V. Ravery, A. Zlotta, P. Dobronski, M. Dobrovits, M. Fakhari, C. Seitz, M. Susani, A. Borkowski, L. Boccon-Gibod, C. C. Schulman, and M. Marberger, "Prospective evaluation

of prostate cancer detected on biopsies 1, 2, 3 and 4: when should we stop?" *J Urol*, vol. 166, no. 5, pp. 1679–1683, Nov 2001.

[10] K. M. Pondman, J. J. Fütterer, B. ten Haken, L. J. Schultze Kool, J. A. Witjes, T. Hambrock, K. J. Macura, and J. O. Barentsz, "MR-guided biopsy of the prostate: an overview of techniques and a systematic review." *Eur Urol*, vol. 54, no. 3, pp. 517–527, Sep 2008. [Online]. Available: http://dx.doi.org/10.1016/j.eururo.2008.06.001

[11] N. Fleshner and L. Klotz, "Role of "saturation biopsy" in the detection of prostate cancer among difficult diagnostic cases." *Urology*, vol. 60, no. 1, pp. 93–97, Jul 2002.

[12] C. Tempany, S. Straus, N. Hata, and S. Haker, "MR-guided prostate interventions." *J Magn Reson Imaging*, vol. 27, no. 2, pp. 356–367, Feb 2008. [Online]. Available: http://dx.doi.org/10.1002/jmri.21259

[13] J. J. Fütterer, S. W. T. P. J. Heijmink, T. W. J. Scheenen, J. Veltman, H. J. Huisman, P. Vos, C. A. Hulsbergen-Van de Kaa, J. A. Witjes, P. F. M. Krabbe, A. Heerschap, and J. O. Barentsz, "Prostate cancer localization with dynamic contrast-enhanced MR imaging and proton MR spectroscopic imaging." *Radiology*, vol. 241, no. 2, pp. 449–458, Nov 2006. [Online]. Available: http://dx.doi.org/10.1148/radiol.2412051866

[14] N. B. Delongchamps, M. Rouanne, T. Flam, F. Beuvon, M. Liberatore, M. Zerbib, and F. Cornud, "Multiparametric magnetic resonance imaging for the detection and localization of prostate cancer: combination of T2-weighted, dynamic contrast-enhanced and diffusion-weighted imaging." *BJU Int*, vol. 107, no. 9, pp. 1411–1418, May 2011. [Online]. Available: http://dx.doi.org/10.1111/j.1464-410X.2010.09808.x

[15] D. Yakar, T. Hambrock, C. Hoeks, J. O. Barentsz, and J. J. Fütterer, "Magnetic resonance-guided biopsy of the prostate: feasibility, technique, and clinical applications." *Top Magn Reson Imaging*, vol. 19, no. 6, pp. 291–295, Dec 2008. [Online]. Available: http://dx.doi.org/10.1097/RMR.0b013e3181aacdb0

[16] A. Heidenreich, P. J. Bastian, J. Bellmunt, M. Bolla, S. Joniau, T. van der Kwast, M. Mason, V. Matveev, T. Wiegel, F. Zattoni, N. Mottet, and European Association of Urology, "EAU guidelines on prostate cancer. Part 1: screening, diagnosis, and local treatment with curative intent-update 2013." *Eur Urol*, vol. 65, no. 1, pp. 124–137, Jan 2014.

[17] A. Bill-Axelson, L. Holmberg, H. Garmo, J. R. Rider, K. Taari, C. Busch, S. Nordling, M. Häggman, S.-O. Andersson, A. Spångberg, O. Andrén, J. Palmgren, G. Steineck, H.-O. Adami, and J.-E. Johansson, "Radical prostatectomy or watchful waiting in early prostate cancer." *N Engl J Med*, vol. 370, no. 10, pp. 932–942, Mar 2014. [Online]. Available: http://dx.doi.org/10.1056/NEJMoa1311593

[18] T. H. van der Kwast, C. Lopes, C. Santonja, C.-G. Pihl, I. Neetens, P. Martikainen, S. Di Lollo, L. Bubendorf, and R. F. Hoedemaeker, members of the pathology committee of the European

Randomised Study of Screening for Prostate Cancer, "Guidelines for processing and reporting of prostatic needle biopsies." *J Clin Pathol*, vol. 56, no. 5, pp. 336–340, May 2003.

[19] R. Hara, Y. Jo, T. Fujii, N. Kondo, T. Yokoyoma, Y. Miyaji, and A. Nagai, "Optimal approach for prostate cancer detection as initial biopsy: prospective randomized study comparing transperineal versus transrectal systematic 12-core biopsy." *Urology*, vol. 71, no. 2, pp. 191–195, Feb 2008. [Online]. Available: http://dx.doi.org/10.1016/j.urology.2007.09.029

[20] A. Takenaka, R. Hara, T. Ishimura, T. Fujii, Y. Jo, A. Nagai, and M. Fujisawa, "A prospective randomized comparison of diagnostic efficacy between transperineal and transrectal 12-core prostate biopsy." *Prostate Cancer Prostatic Dis*, vol. 11, no. 2, pp. 134–138, 2008. [Online]. Available: http://dx.doi.org/10.1038/sj.pcan.4500985

[21] S. W. T. P. J. Heijmink, H. van Moerkerk, L. A. L. M. Kiemeney, J. A. Witjes, F. Frauscher, and J. O. Barentsz, "A comparison of the diagnostic performance of systematic versus ultrasound-guided biopsies of prostate cancer." *Eur Radiol*, vol. 16, no. 4, pp. 927–938, Apr 2006. [Online]. Available: http://dx.doi.org/10.1007/s00330-005-0035-y

[22] C. R. King, J. E. McNeal, H. Gill, and J. C. Presti, Jr, "Extended prostate biopsy scheme improves reliability of Gleason grading: implications for radiotherapy patients." *Int J Radiat Oncol Biol Phys*, vol. 59, no. 2, pp. 386–391, Jun 2004. [Online]. Available: http://dx.doi.org/10.1016/j.ijrobp.2003.10.014

[23] T. Penzkofer and C. M. Tempany-Afdhal, "Prostate cancer detection and diagnosis: the role of MR and its comparison with other diagnostic modalities–a radiologist's perspective." *NMR Biomed*, vol. 27, no. 1, pp. 3–15, Jan 2014. [Online]. Available: http://dx.doi.org/10.1002/nbm.3002

[24] M. de Rooij, E. H. J. Hamoen, J. J. Fütterer, J. O. Barentsz, and M. M. Rovers, "Accuracy of multiparametric MRI for prostate cancer detection: a meta-analysis." *AJR Am J Roentgenol*, vol. 202, no. 2, pp. 343–351, Feb 2014. [Online]. Available: http://dx.doi.org/10.2214/AJR.13.11046

[25] B. Turkbey, H. Mani, V. Shah, A. R. Rastinehad, M. Bernardo, T. Pohida, Y. Pang, D. Daar, C. Benjamin, Y. L. McKinney, H. Trivedi, C. Chua, G. Bratslavsky, J. H. Shih, W. M. Linehan, M. J. Merino, P. L. Choyke, and P. A. Pinto, "Multiparametric 3 T prostate magnetic resonance imaging to detect cancer: histopathological correlation using prostatectomy specimens processed in customized magnetic resonance imaging based molds." *J Urol*, vol. 186, no. 5, pp. 1818–1824, Nov 2011. [Online]. Available: http://dx.doi.org/10.1016/j.juro.2011.07.013

[26] C. M. Moore, N. L. Robertson, N. Arsanious, T. Middleton, A. Villers, L. Klotz, S. S. Taneja, and M. Emberton, "Image-guided prostate biopsy using magnetic resonance imaging-derived

targets: a systematic review." *Eur Urol*, vol. 63, no. 1, pp. 125–140, Jan 2013. [Online]. Available: http://dx.doi.org/10.1016/j.eururo.2012.06.004

[27] D. Beyersdorff, A. Winkel, B. Hamm, S. Lenk, S. A. Loening, and M. Taupitz, "MR imaging-guided prostate biopsy with a closed MR unit at 1.5 T: initial results." *Radiology*, vol. 234, no. 2, pp. 576–581, Feb 2005. [Online]. Available: http://dx.doi.org/10.1148/radiol.2342031887

[28] A. G. Anastasiadis, M. P. Lichy, U. Nagele, M. A. Kuczyk, A. S. Merseburger, J. Hennenlotter, S. Corvin, K.-D. Sievert, C. D. Claussen, A. Stenzl, and H.-P. Schlemmer, "MRI-guided biopsy of the prostate increases diagnostic performance in men with elevated or increasing PSA levels after previous negative TRUS biopsies." *Eur Urol*, vol. 50, no. 4, pp. 738–48; discussion 748–9, Oct 2006. [Online]. Available: http://dx.doi.org/10.1016/j.eururo.2006.03.007

[29] M. R. Pokorny, M. de Rooij, E. Duncan, F. H. Schröder, R. Parkinson, J. O. Barentsz, and L. C. Thompson, "Prospective study of diagnostic accuracy comparing prostate cancer detection by transrectal ultrasound-guided biopsy versus magnetic resonance (MR) imaging with subsequent MR-guided biopsy in men without previous prostate biopsies." *Eur Urol*, vol. 66, no. 1, pp. 22–29, Jul 2014. [Online]. Available: http://dx.doi.org/10.1016/j.eururo.2014.03.002

[30] T. Hambrock, J. J. Fütterer, H. J. Huisman, C. Hulsbergen-vandeKaa, J.-P. van Basten, I. van Oort, J. A. Witjes, and J. O. Barentsz, "Thirty-two-channel coil 3 T magnetic resonance-guided biopsies of prostate tumor suspicious regions identified on multimodality 3 T magnetic resonance imaging: technique and feasibility." *Invest Radiol*, vol. 43, no. 10, pp. 686–694, Oct 2008. [Online]. Available: http://dx.doi.org/10.1097/RLI.0b013e31817d0506

[31] ASTM International, "F2052-06: Standard test method for measurement of magnetically induced displacement force on medical devices in the magnetic resonance environment," 2006.

[32] B. Kogelman, "Treatment planning in focal laser ablation: increase of efficiency of MR-guided procedures," *Master Thesis Technical Medicine*, 2013.

[33] A. Mottrie and V. Ficarra, "Can robot-assisted radical prostatectomy still be considered a new technology pushed by marketers? The IDEAL evaluation." *Eur Urol*, vol. 58, no. 4, pp. 525–527, Oct 2010. [Online]. Available: http://dx.doi.org/10.1016/j.eururo.2010.07.033

[34] J. I. Epstein, M. Amin, L. Boccon-Gibod, L. Egevad, P. A. Humphrey, G. Mikuz, D. Newling, S. Nilsson, W. Sakr, J. R. Srigley, T. M. Wheeler, and R. Montironi, "Prognostic factors and reporting of prostate carcinoma in radical prostatectomy and pelvic lymphadenectomy specimens." *Scand J Urol Nephrol Suppl*, no. 216, pp. 34–63, May 2005. [Online]. Available: http://dx.doi.org/10.1080/03008880510030932

[35] O. Yossepowitch, A. Bjartell, J. A. Eastham, M. Graefen, B. D. Guillonneau, P. I. Karakiewicz, R. Montironi, and F. Montorsi, "Positive surgical margins in radical prostatectomy: outlining the problem and its long-term consequences." *Eur Urol*, vol. 55, no. 1, pp. 87–99, Jan 2009. [Online]. Available: http://dx.doi.org/10.1016/j.eururo.2008.09.051

[36] O. Yossepowitch, A. Briganti, J. A. Eastham, J. Epstein, M. Graefen, R. Montironi, and K. Touijer, "Positive surgical margins after radical prostatectomy: a systematic review and contemporary update." *Eur Urol*, vol. 65, no. 2, pp. 303–313, Feb 2014. [Online]. Available: http://dx.doi.org/10.1016/j.eururo.2013.07.039

[37] G. Novara, V. Ficarra, S. Mocellin, T. E. Ahlering, P. R. Carroll, M. Graefen, G. Guazzoni, M. Menon, V. R. Patel, S. F. Shariat, A. K. Tewari, H. Van Poppel, F. Zattoni, F. Montorsi, A. Mottrie, R. C. Rosen, and T. G. Wilson, "Systematic review and meta-analysis of studies reporting oncologic outcome after robot-assisted radical prostatectomy." *Eur Urol*, vol. 62, no. 3, pp. 382–404, Sep 2012. [Online]. Available: http://dx.doi.org/10.1016/j.eururo.2012.05.047

[38] P. Puech, A. Villers, A. Ouzzane, and L. Lemaitre, "Prostate cancer: diagnosis, parametric imaging and standardized report." *Diagn Interv Imaging*, vol. 95, no. 7-8, pp. 743–752, 2014. [Online]. Available: http://dx.doi.org/10.1016/j.diii.2014.06.012

[39] J. Y. Kim, S. H. Kim, Y. H. Kim, H. J. Lee, M. J. Kim, and M. S. Choi, "Low-risk prostate cancer: the accuracy of multiparametric mr imaging for detection." *Radiology*, vol. 271, no. 2, pp. 435–444, May 2014. [Online]. Available: http://dx.doi.org/10.1148/radiol.13130801

[40] B. Turkbey, P. A. Pinto, H. Mani, M. Bernardo, Y. Pang, Y. L. McKinney, K. Khurana, G. C. Ravizzini, P. S. Albert, M. J. Merino, and P. L. Choyke, "Prostate cancer: value of multiparametric MR imaging at 3 T for detection–histopathologic correlation." *Radiology*, vol. 255, no. 1, pp. 89–99, Apr 2010. [Online]. Available: http://dx.doi.org/10.1148/radiol.09090475

[41] E. Gibson, C. Crukley, M. Gaed, J. A. Gómez, M. Moussa, J. L. Chin, G. S. Bauman, A. Fenster, and A. D. Ward, "Registration of prostate histology images to ex vivo MR images via strand-shaped fiducials." *J Magn Reson Imaging*, vol. 36, no. 6, pp. 1402–1412, Dec 2012. [Online]. Available: http://dx.doi.org/10.1002/jmri.23767

[42] S. Y. Kimm, T. V. Tarin, J. H. Lee, B. Hu, K. Jensen, D. Nishimura, and J. D. Brooks, "Methods for registration of magnetic resonance images of ex vivo prostate specimens with histology." *J Magn Reson Imaging*, vol. 36, no. 1, pp. 206–212, Jul 2012. [Online]. Available: http://dx.doi.org/10.1002/jmri.23614

[43] G. Nir, R. S. Sahebjavaher, P. Kozlowski, S. D. Chang, R. Sinkus, S. L. Goldenberg, and S. E. Salcudean, "Model-based registration of ex vivo and in vivo MRI of the prostate using elastography*." *IEEE Trans Med Imaging*, vol. 32, no. 7, pp. 1349–1361, Jul 2013. [Online]. Available: http://dx.doi.org/10.1109/TMI.2013.2269174

[44] X. Fan, C. R. Haney, G. Agrawal, C. A. Pelizzari, T. Antic, S. E. Eggener, I. Sethi, J. N. River, M. Zamora, G. S. Karczmar, and A. Oto, "High-resolution MRI of excised human prostate specimens acquired with 9.4 T in detection and identification of cancers: validation

of a technique." *J Magn Reson Imaging*, vol. 34, no. 4, pp. 956–961, Oct 2011. [Online]. Available: http://dx.doi.org/10.1002/jmri.22745

[45] G. Hatzichristodoulou, S. Wagenpfeil, G. Weirich, M. Autenrieth, T. Maurer, M. Thalgott, T. Horn, M. Heck, K. Herkommer, J. E. Gschwend, and H. Kübler, "Intraoperative frozen section monitoring during nerve-sparing radical prostatectomy: evaluation of partial secondary resection of neurovascular bundles and its effect on oncologic and functional outcome." *World J Urol*, Jun 2015. [Online]. Available: http://dx.doi.org/10.1007/s00345-015-1623-3

[46] T. Schlomm, P. Tennstedt, C. Huxhold, T. Steuber, G. Salomon, U. Michl, H. Heinzer, J. Hansen, L. Budäus, S. Steurer, C. Wittmer, S. Minner, A. Haese, G. Sauter, M. Graefen, and H. Huland, "Neurovascular structure-adjacent frozen-section examination (neurosafe) increases nerve-sparing frequency and reduces positive surgical margins in open and robot-assisted laparoscopic radical prostatectomy: experience after 11,069 consecutive patients." *Eur Urol*, vol. 62, no. 2, pp. 333–340, Aug 2012. [Online]. Available: http://dx.doi.org/10.1016/j.eururo.2012.04.057

[47] B. Saracino, M. Gallucci, P. De Carli, A. Soriani, R. Papalia, S. Marzi, V. Landoni, M. G. Petrongari, S. Arcangeli, E. Forastiere, S. Sentinelli, and G. Arcangeli, "Phase I-II study of intraoperative radiation therapy (iort) after radical prostatectomy for prostate cancer." *Int J Radiat Oncol Biol Phys*, vol. 71, no. 4, pp. 1049–1056, Jul 2008. [Online]. Available: http://dx.doi.org/10.1016/j.ijrobp.2007.11.076

Appendices

Appendix A

Determination of the pivot of the needle guide

This appendix describes the test that was performed to determine the pivot, or centre of rotation, of the needle guide when attached to the biopsy device as used during the MR guided biopsy procedure. Definition of this point is important as it forms a point of the needle guide that will always be visible in the real-time MR images independent of the orientation of the needle guide. Otherwise, visual feedback of the orientation could be lost.

In order to discover the pivot, multiple MRI scans using a TRUFI sequence were acquired of the needle guide attached to the biopsy device which was oriented into different angles, this could be done precisely because the device contains local protractors. In the first session, the needle guide was consecutively orientated 0, 5, 10, and 15 degrees downward by loosening setscrew 1 (figure 5.4) and adjust the loosened part of the biopsy device upward. In a separate session, with the up-down adjustment equal back to zero again, the same angular deflections were applied to adjust the needle guide to the right. This was achieved by loosening setscrew 2 (figure 5.4) and turning the loosened part of device around its own axis.

Both a sagittal and a coronal image were acquired from the needle guide in each different angular deflection so that in total four sets of four images each, were obtained. In a Matlab script, a line was manually draw alongside the centre of the needle guide for each image and the four resulting lines were simultaneously projected on the final image of a set. By drawing a line between the tip of the needle guide and the intersection of the previously drawn lines the distance of the pivot relative to the needle tip was calculated. The distance was determined twice using the coronal images acquired for monitoring the angular changes in the left-right direction and the sagittal images acquired for monitoring the change in the up-down direction. The other two sets served as a control to verify that the adjustments had influence in one degree of freedom only. If this is the case all four drawn lines should run parallel to each other.

Performing the described measurements in Matlab resulted in a pivot position of 89.3 mm based on the sagittal images of the up-down adjustment and of 86.2 mm based on the coronal images of the left-right adjustments. This resulted in a mean of 87.7 mm. See figure A.1.

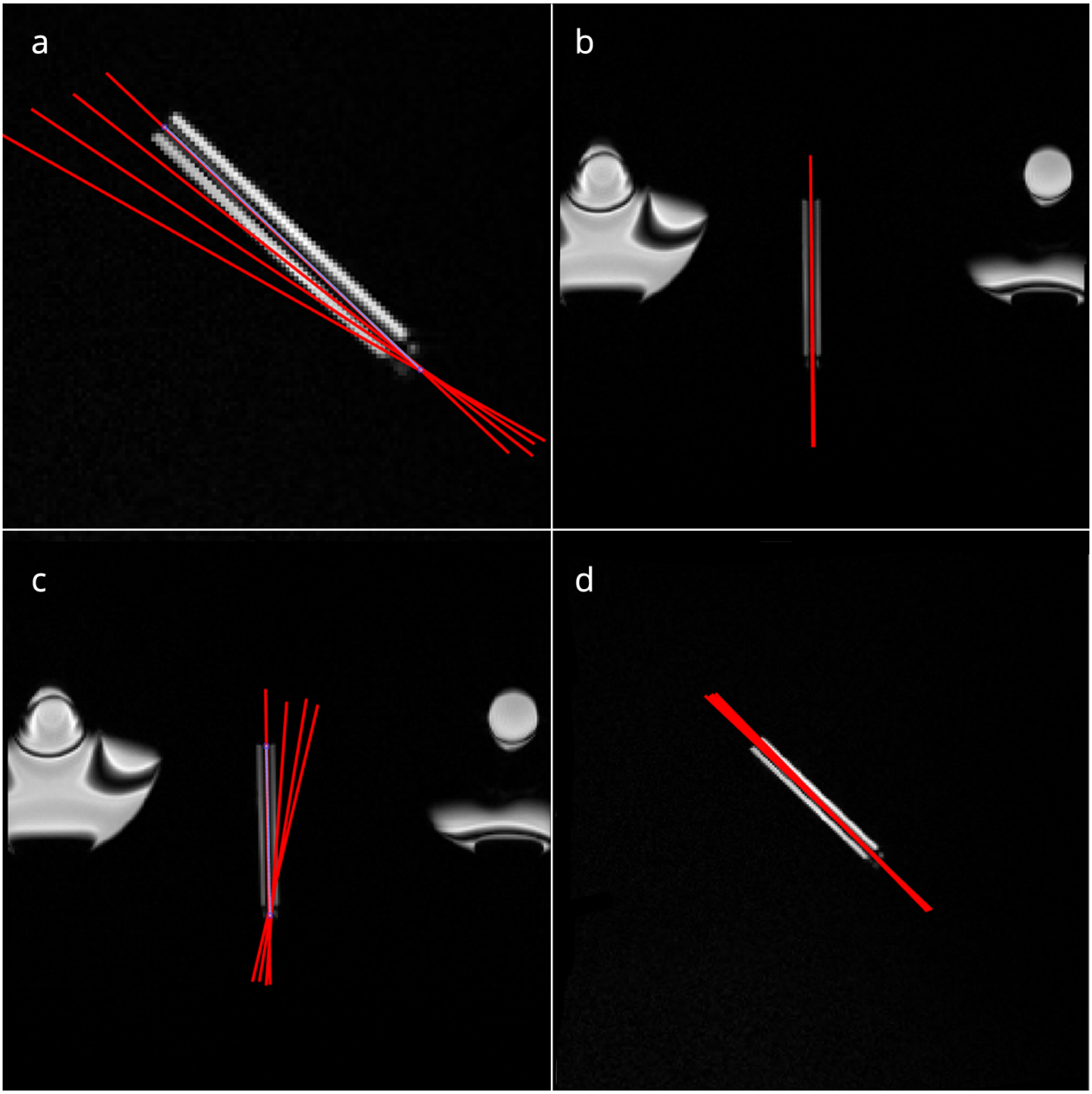

Figure A.1: In quadrant **(a)**, determination of the pivot position based on the sagittal images acquired when performing up-down adjustment. The pivot is positioned at the intersection of all four red lines. The image is slightly zoomed in.; **(b)**, the coronal images of acquired during up-down movement. Note that the four red lines are running parallel to each other.;**(c)**, the pivot position visible in the coronal images acquired during left-right adjustment.;**(d)** Again four parallel running lines, now in the sagittal image during left-right adaptation.

Appendix B

A comprehensive manual to IFE

This section provides a comprehensive manual to IFE as it was applied during the MR guided prostate biopsies using a real-time sequence and in-room visualisation using an MTD. It mainly addresses the required manual adjustments of the imaging planes such that these can be applied to orientate the needle guide in the direction of the CSR.

Once T2W images of the region of interest (ROI) covering the prostate (in this example the phantom) and the entire needle guide are acquired, these are transferred from the MR host to the dedicated IFE PC using a built-in transfer script. This comes down to transferring the images to a shared folder on the MR host which is accessible by the IFE PC. With IFE in *planning mode*, the stack of 2D, more or less axial, images is digitally augmented to a multi plane view of the ROI: the already available axial view, plus a coronal and sagittal view.

Subsequently, the CSR can be defined by setting a *target* point. This can be done at best using the axial images as these provide the highest resolution regarding the fact that the pixels of the T2W-images are not cubic. Using the sagittal view, the coronal slice can be toggled and rotated in such a way that is positioned both alongside the needle guide as well as at the centre of it. Using the build-in measurement tool the position of the *entry* point is marked at the the pivot of the needle guide. The pivot was experimentally determined at 9.0 cm (87.7 mm) from the leading edge of the contrast-filled compartment. The performed adjustments so far are depicted in figure B.1.

The centres of the coronal and sagittal slice are positioned over the marked entry point. Next, both slices are rotated until they display both the target and entry point under the condition that each slice is rotated around one axis only. To the achieve this, the coronal slice was rotated in the sagittal image, thus around the sagittal axis. Likewise, the sagittal slice was rotated in the axial image, thus around the axial axis. This specific way planning of the MRI slices allows visualisation of the adjustments of the needle guide of one degree of freedom per viewing window. So, in this case, adjustments of the needle guide in the top-down direction are visualised in the sagittal imaging slice, whereas the adjustments in the left-right direction are visualised in the coronal imaging slice.

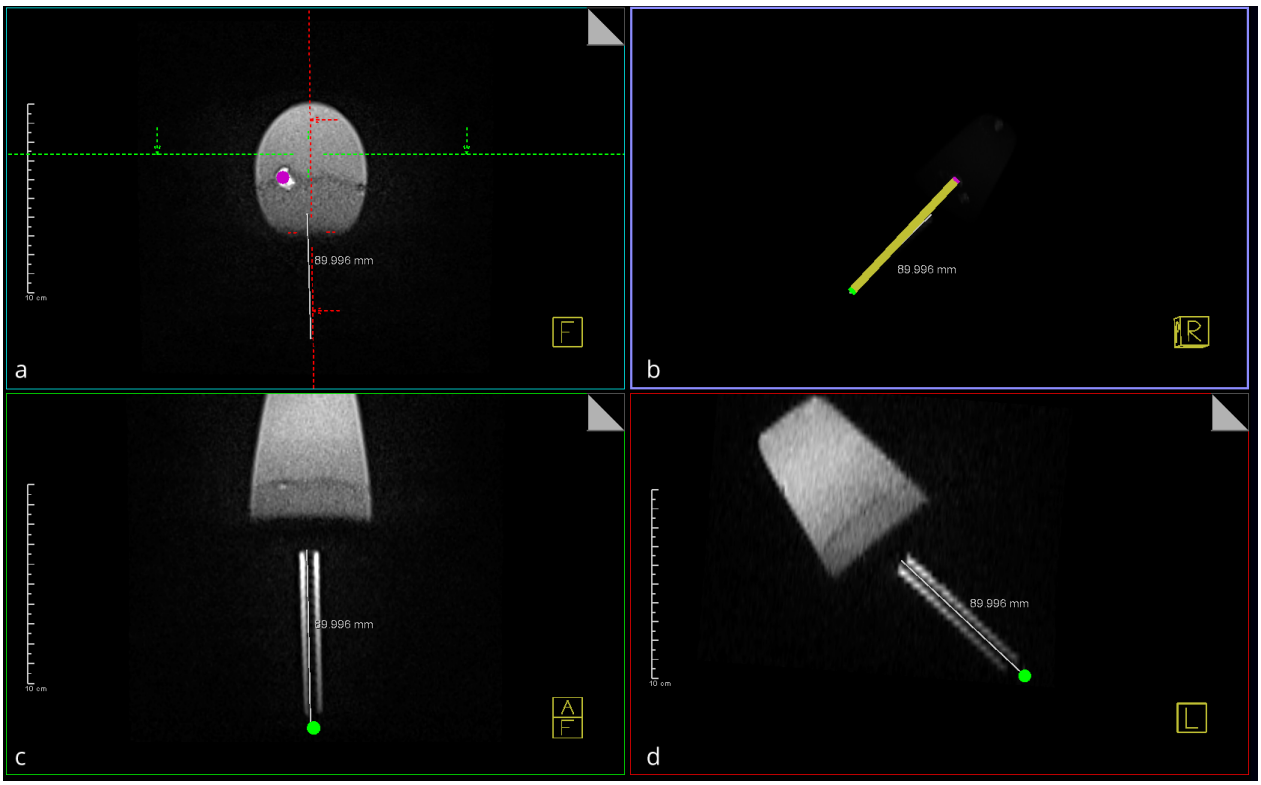

Figure B.1: In quadrant **(a)**, the axial T2W MRI of the phantom. In purple the target point on top of CSR which is partially visible as a hyper intense area. The striped green and red line are the positions of the coronal and sagittal slice respectively; **(b)**, 3D representation showing the planned needle trajectory in yellow. The phantom only appears vaguely as the image contrast could not be altered as a result of a bug; **(c)**, the initially coronal MRI of the phantom is now aligned with the needle guide by pivoting it around the sagittal axes. Besides that it is toggled to the centre of the device. The green dot is the entry point which has been measured and positioned at 9.0 cm from the needle tip; and **(d)** the sagittal view.

Figure B.2 shows the final result of slice planning in IFE.

Once the planning is satisfactory, it is transferred to the MR host where the slices of the BEAT-iRTTT sequence are positioned and oriented accordingly. Meanwhile, IFE is switched from planning mode to *standard mode* and the viewing windows are set to *scan*. Furthermore, the layout is set to a three 2D plus 3D 2×2 layout and the reference lines are switched off. Next, the imaging sequence can be started, and the acquired images are visualised on the IFE PC and on the remote-desktop-connected MTD which is positioned in the MR room (see 6.1 for the set-up). By applying the visual information from the coronal and sagittal slice, the operator adjusts the needle guide in the left-right direction and top-bottom respectively until it is in-plane with each of the slices. Figure B.3 shows the screen that is presented on the in-room MTD.

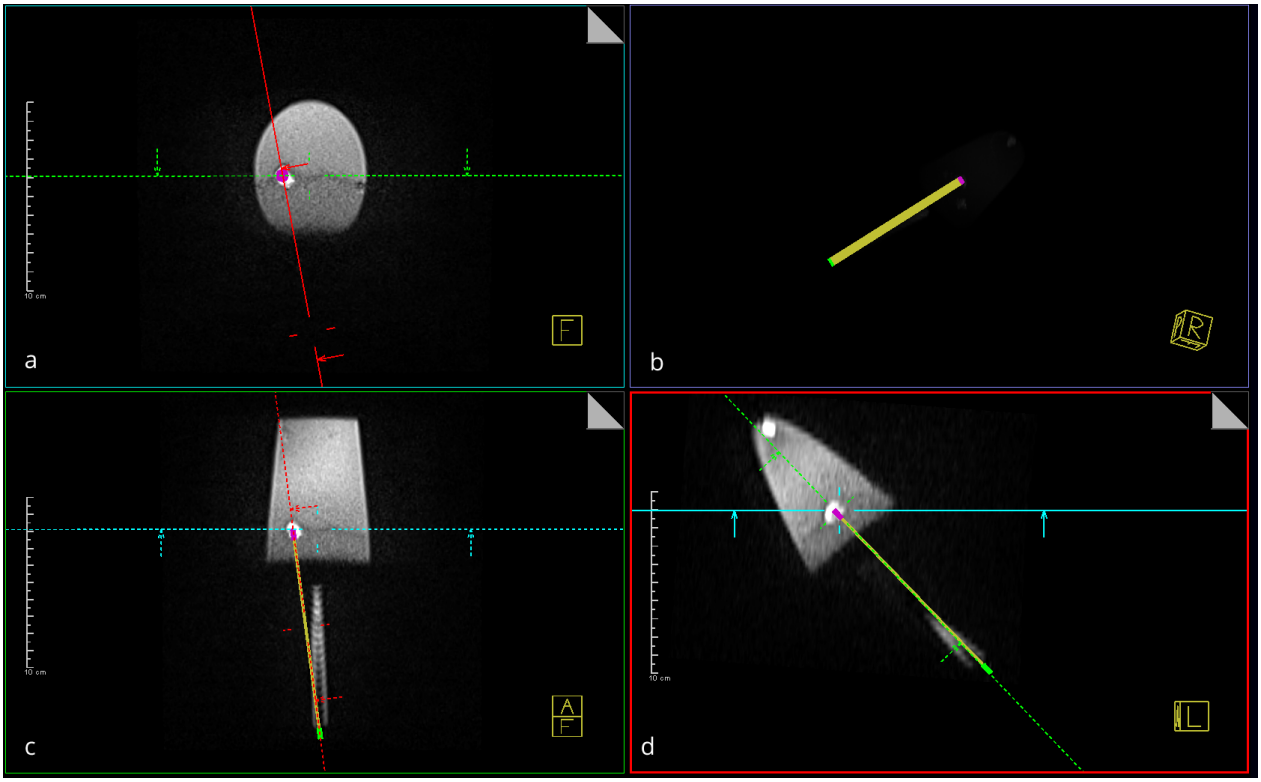

Figure B.2: In quadrant **(a)**, again the axial T2W MRI of the phantom; **(b)**, the 3D representation; **(c)**, subsequent to the aforementioned adjustments the coronal slice is now aligned with the needle trajectory planning by rotating it around the sagittal axis at which its pivot is positioned at the turning point of the needle. Since this window is visualising the left-right adjustments of the needle guide, it becomes clear that the guide show be adjusted slightly to the left (according to the window axes system); and **(d)** the sagittal MRI slice which was subjected to similar adjustments as the coronal slice, except that is was rotated around the axial axis. According to the window axis the needle guide requires almost no adjustment.

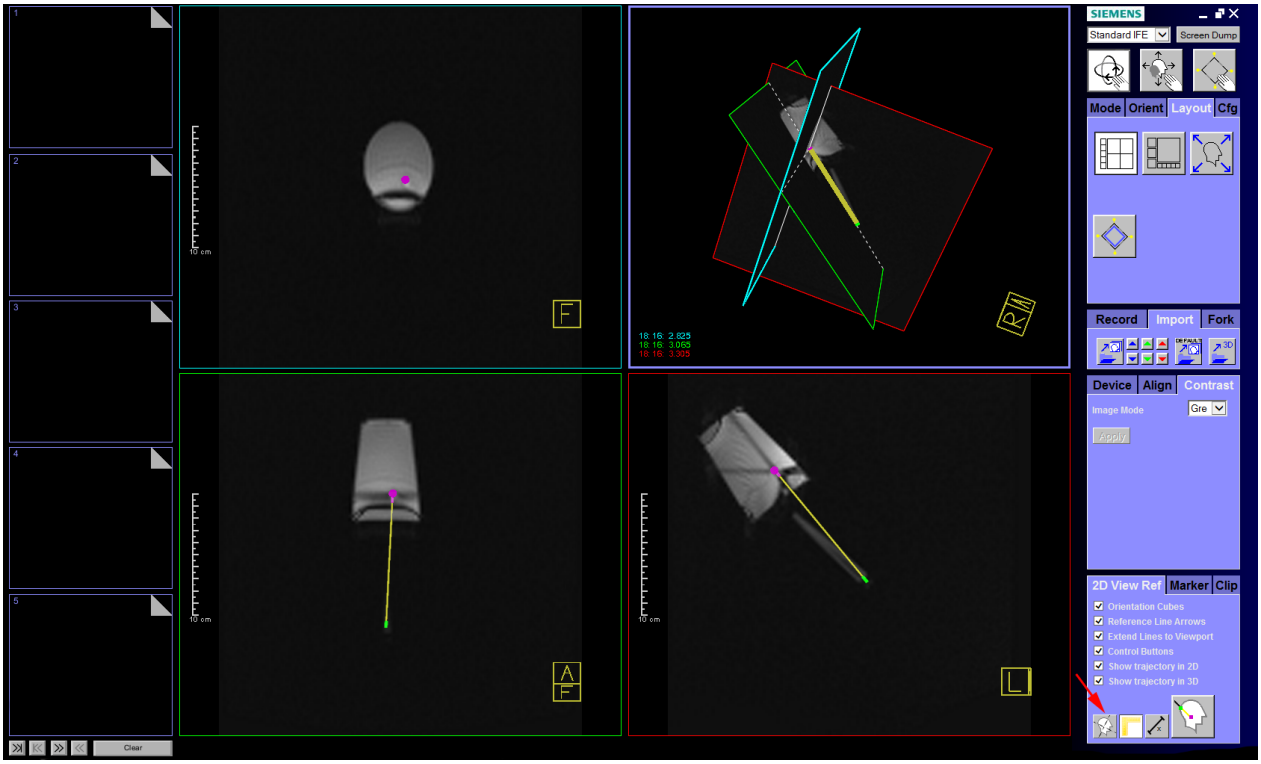

Figure B.3: Now in *standard IFE* mode, but using a similar set-up as in the previous images, the planned needle trajectory, yellow, is projected as an overlay on the axial, coronal, and sagittal images that were acquired using the BEAT-iRTTT sequence. By clicking on the white highlighted icon under the *layout* tab on the right the three 2D plus 3D 2×2 layout is obtained. The reference lines are removed by clicking on the icon pointed out by the red arrow under the *2D view ref* tab.

Appendix C

Description of the Matlab GUI used to calculate needle deviation

The accuracy of the real-time MR guided prostate biopsy procedure was calculated using a Matlab GUI which is visualised in figure C.1 This chapter will give a brief description on how to operate the GUI and will give a short description on the calculation that are performed underwater.

The first step is to load the confirmation TRUFI images, per "biopsy" session 5 axial images to investigate the left-right deviation and 5 sagittal images to investigate the up-down deviation were acquired. Loading is done by pressing the *Load Images* button (1), this will pop-up a windows explorer screen by which one is able to navigate to the desired set of images. A set images has to be stored in a separate file folder. No two sets can be stored in the same folder, as the loading function is not equipped with a function to separate the sets of confirmation images acquired for different biopsy sessions. Once the folder containing the desired image set to be analysed has is selected the loading function automatically displays the axial images and sagittal images in their separate image window in the GUI, with axial ones displayed in the window on the left (a) and the sagittal images displayed in the right window (b). If the *Load Images* button is clicked once again, another image set can be loaded

The next task is to determine the centre of the lesion and the centre of the needle guide, this can be done by navigating through the stack of images using the slider on the left of each image window. Once the centre of the lesion is determined it can be marked by clicking the *Get Target Position* button (2) that lets a marker cross appear. By double clicking the centre of the lesion within the image its coordinates are stored and the position is marked by a green dot. In case of a mistake, the user can correct by clicking button 2 again and re-define the centre of the lesion.

After marking the lesion's centre, the trajectory of the needle must be determined. If necessary a different image can be selected using the slider again to find the centre of the needle guide. After clicking the *Get Trajectory* button (3), the user must draw a rough line between the two white

bars of the needle guide. The line is confirmed by double clicking on it, which will also activate a repositioning algorithm. Using an intensity profile, this algorithm detects the two white intensity peaks orthogonally at the left and the right of both ends (position A and B) of the manually drawn line. The middle of the line between both peaks is the centre of the needle guide (the single black stoke) and thus the needle trajectory. The coordinates of the trajectory are stored and it is automatically drawn in blue while artificially increasing its length so that it is easily visible whether the needle hit the lesion or not. Again, mistakes can be corrected by re-clicking the *Get Trajectory* button.

As final step the *Calculate Distance* button (4) can be pressed that will automatically calculated the shortest distance between the centre of the lesion and the needle trajectory. The distance is displayed in the window under (5).

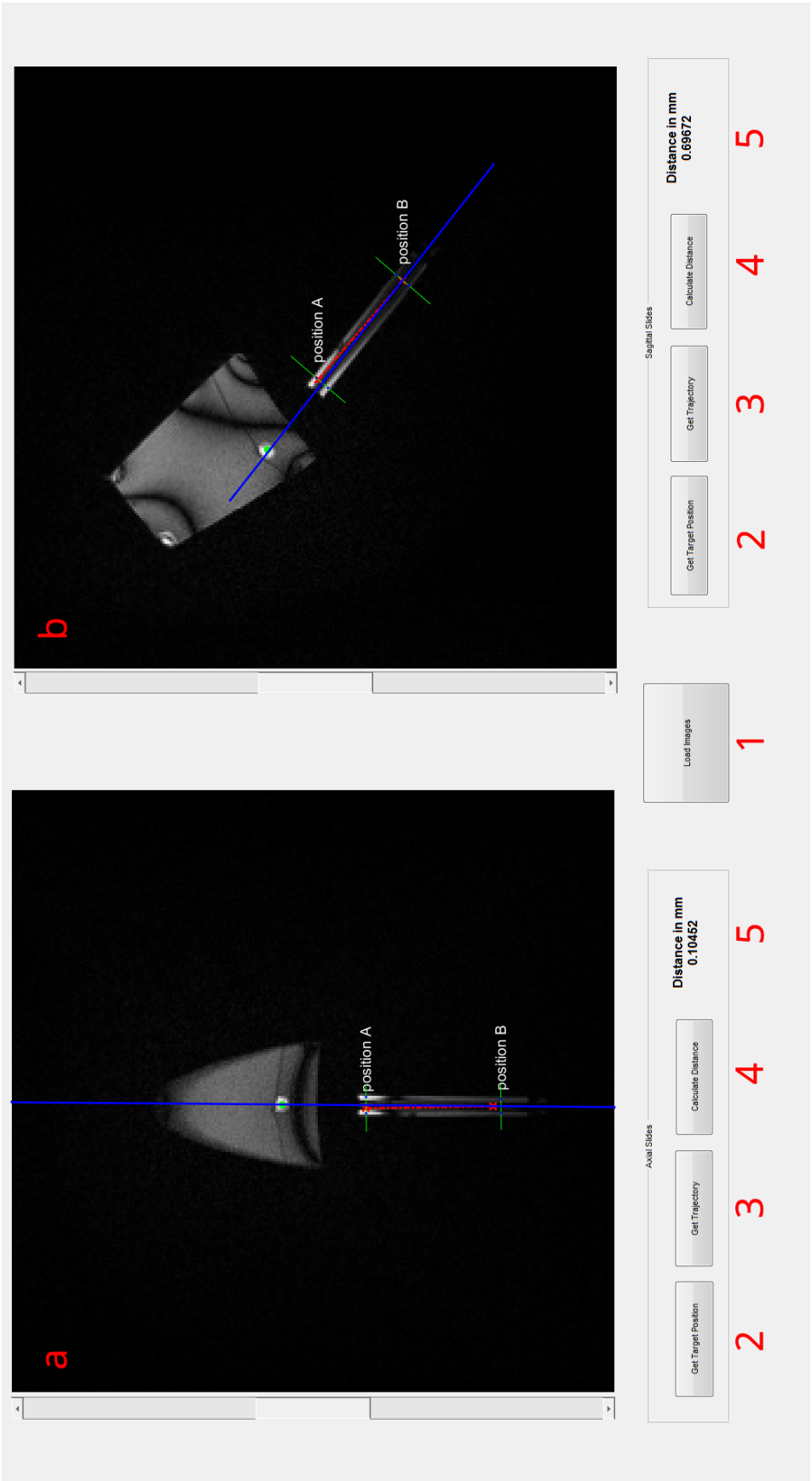

Figure C.1: Screen print of the Matlab GUI programmed to calculate the needle deviation on behalf of the accuracy study